JGR Solid Earth

RESEARCH ARTICLE
10.1029/2022JB024434

# Rotational Extension Promotes Coeval Upper Crustal Brittle Faulting and Deep-Seated Rift-Axis Parallel Flow: Dynamic Coupling Processes Inferred From Analog Model Experiments

**Timothy Chris Schmid**[1], **Guido Schreurs**[1], **and Jürgen Adam**[2]

[1]Institute of Geological Sciences, University of Bern, Bern, Switzerland, [2]Department of Earth Sciences, Royal Holloway, University of London, Egham, United Kingdom

**Key Points:**

- We use volumetric and surface image correlation techniques to depict coeval brittle rifting and ductile flow patterns in analog models
- Rotational rifting promotes rift-axis parallel lateral flow, causing outflow of lower crustal material away from the rotation axis
- Partial coupling of rift-axis parallel displacements in the brittle and viscous domain is transient and dynamic over time

**Correspondence to:**
T. C. Schmid,
timothy.schmid@geo.unibe.ch

**Citation:**
Schmid, T. C., Schreurs, G., & Adam, J. (2022). Rotational extension promotes coeval upper crustal brittle faulting and deep-seated rift-axis parallel flow: Dynamic coupling processes inferred from analog model experiments. *Journal of Geophysical Research: Solid Earth*, *127*, e2022JB024434. https://doi.org/10.1029/2022JB024434

Received 22 MAR 2022
Accepted 22 JUL 2022

**Author Contributions:**
**Conceptualization:** Timothy Chris Schmid
**Data curation:** Timothy Chris Schmid
**Formal analysis:** Timothy Chris Schmid
**Funding acquisition:** Guido Schreurs
**Investigation:** Timothy Chris Schmid
**Methodology:** Timothy Chris Schmid, Jürgen Adam
**Project Administration:** Guido Schreurs
**Supervision:** Guido Schreurs, Jürgen Adam
**Visualization:** Timothy Chris Schmid
**Writing – original draft:** Timothy Chris Schmid
**Writing – review & editing:** Guido Schreurs, Jürgen Adam



**Abstract** The lower parts of warm, thick continental crust can flow in a ductile fashion to accommodate thinning of the upper brittle crust during extension. Naturally occurring continental rifts with a rift-axis parallel deformation gradient imply an underlying rotational component. In such settings, rift-parallel crustal flow transports material perpendicular to the direction of rifting. We use analog experiments to investigate rotational rifting and coeval crustal flow. To test the effect of rift-axis parallel flow on rift evolution, we use different gravitational loads resulting in a range of horizontal pressure gradient magnitudes which drive horizontal lower-crustal flow. The use of (three dimensional) 3D Digital Volume Correlation techniques on X-ray CT data combined with 3D Digital Image Correlation techniques applied to topographic stereo images provides detailed insights on the contemporaneous evolution of ductile flow patterns and brittle rift structures, respectively. Our results depict a complex flow field in the ductile lower crust during rotational rifting with: (a) extension-parallel horizontal inward flow and vertical upward flow that compensates thinning of the brittle upper crustal layer; (b) rift-axis parallel lateral flow, that compensates greater amounts of thinning further away from the rotation axis; and (c) different degrees of mechanical coupling between the brittle and viscous layers that change during rift propagation. Our analog experiments provide insights into ductile lower crustal flow patterns during rift evolution. The results emphasize the three dimensionality of rifting, which is an important effect that should be considered when estimating the amount of crustal extension from two dimensional (2D) cross sections.

**Plain Language Summary** Stretching of continental plates produces rifts, that are characterized by narrow fault zones in the brittle, upper parts of the Earth's crust and flow of rocks in the more ductile, lower parts of the crust. As rifts often propagate in one direction, the flow pattern in the lower crust can be complex and challenging to study and interpret. Here, we use laboratory experiments to investigate flow in propagating rifts. The application of X-ray CT-scanning allows us not only to visualize the model internal deformation, but also to quantify the deformation which provides detailed insights into the coeval evolution of ductile flow patterns and brittle rift structures. Our results document a complex 3D flow pattern within the lower crust with an important component along the rift axis, emphasizing the need to consider the evolution of rifts in 3D.

## 1. Introduction

During continental rifting, extension in the upper parts of the crust is accommodated by brittle faulting. If stretching is distributed evenly throughout the crust (McKenzie, 1978), faulting in the upper crust is balanced by ductile deformation in the lower crust (e.g., Buck, 1991; Kusznir & Karner, 2007). However, at passive margins, subsidence analyzed from geological cross sections differs from expected values when applying the McKenzie uniform stretching model. Such observations led to the development of depth-dependent stretching models (Wernicke, 1985) that account for higher amounts of extension in lower parts of the crust, which permit larger subsidence values. More recent studies of passive margins have suggested ductile crustal flow as an alternative mechanism for removal of lower crustal material. Consequently, mass is not conserved in 2D plane-strain cross sections, which can explain discrepancies between estimated amounts of extension in the upper- and lower crust (P. D. Clift, 2015).

Ductile flow in the lower crust should also occur in intracontinental rift settings. Indeed, lower crustal flow is expected in extensional settings where the crustal thickness exceeds 20 km and the upper mantle is strong (McKenzie et al., 2000 and references therein). This phenomenon has been extensively demonstrated in the Basin and Range Province, where flow of the lower crust toward the rift center compensates lateral crustal thickness

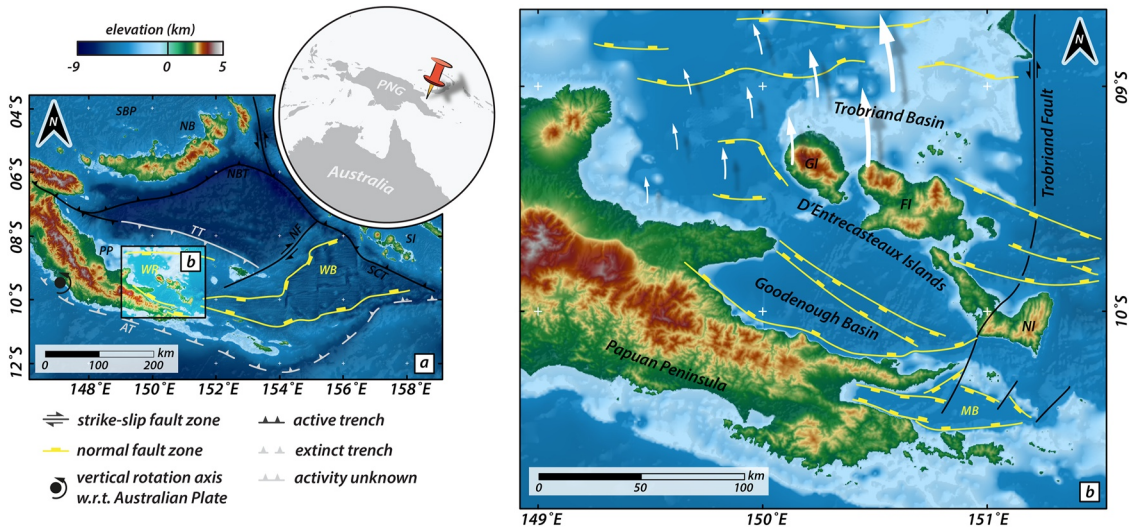


**Figure 1.** Westward propagation of the oceanic Woodlark Basin (WB) and the continental Woodlark Rift (WR) into the Papuan Peninsula (PP). (a) Tectonic setting of eastern Papua New Guinea: SBP, South Bismarck Plate, NB, New Britain, NBT, New Britain Trench, SI, Solomon Islands, SCT, San Cristobal Trench, NF, Nubura Fault, AT, Aure Trough, TT, Trobriand Trough. The opening of the Woodlark Basin and Woodlark Rift can be described by a rotation around a vertical rotation axis with decreasing spreading rates toward the West. (b) Zoom in of the Woodlark Rift and subbasins. The emerged Metamorphic Core Complex of the D'Entrecasteaux Islands divides the Woodlark Rift into a northern (Trobriand Basin) and a southern (Goodenough Basin) part. GI, Goodenough Island, FI, Fergusson Island, NI, Normanby Island, MB, Milne Bay, and vectors indicate the rotational velocity field. Topography and bathymetry are obtained from the General Bathymetric Chart of the Oceans GEBCO (2021). Modified after Little et al. (2011), Miller et al. (2012), and Wallace et al. (2014).

variations (e.g., Buck, 1991; Kruse et al., 1991; Zuber et al., 1986). However, after extension ceases, lateral ductile flow may halt and reverse its direction (i.e., away from the rift center) due to increasing sediment loading (e.g., Morley & Westaway, 2006; P. Clift et al., 2002; P. D. Clift, 2015; P. D. Clift et al., 2015; Westaway, 1994). While most of these studies focus on ductile flow in two-dimensions, the out-of-plane component (i.e., rift-axis parallel) should not be neglected. Especially in rift settings with an underlying extension gradient, rift-axis parallel ductile flow may compensate for increased thinning along the rift axis (Amato et al., 2004; Gautier et al., 2008; MacCready et al., 1997).

Three-dimensional crustal flow during extension has been demonstrated in the D'Entrecasteaux Islands in the Woodlark Rift (Figure 1) by Little et al. (2007, 2011, 2013). The Woodlark Rift is a continental rift zone east of the Papuan Peninsula separating the Australian plate from the Woodlark Microplate. To the east, the Woodlark Rift is confined by the west-propagating oceanic Woodlark Basin. At the transition between continental and oceanic crust (i.e., near the Moresby Seamount), continental breakup occurs along a characteristic V-shaped rift zone, with respect to the rift margin boundary faults (Benes et al., 1994; Taylor et al., 1999). This specific type of continent-ocean boundary can be attributed to a counter-clockwise rotation of the Woodlark Plate (e.g., Wallace et al., 2014 and references therein). Based on GPS measurements, maximum opening velocities at the eastern end of the Woodlark rift are around 20 mm/a (Wallace et al., 2004) but, based on magnetic anomalies in the Woodlark Basin, were faster between 3.6 and 0.5 Ma (Taylor et al., 1999). The Woodlark Rift is bounded by a south-dipping boundary fault in the north and the north-dipping Goodenough Fault near the ca. 3 km high Papuan Orogen in the south (Little et al., 2011). Several metamorphic core complexes within the Woodlark Rift, among it the D'Entrecasteaux Islands, are indicative of its continental origin (Wallace et al., 2014) and document lower crustal flow (Little et al., 2007, 2011, 2013). A flat Moho at a depth of 20–30 km (Abers et al., 2002) indicates that the lower crust must have had a low enough viscosity to allow ductile rift-axis normal flow to compensate lateral pressure gradients (Little et al., 2007; Westaway, 2005). In addition, rift-axis parallel flow may explain excess subsidence when comparing observed and modeled bathymetric transects across the Woodlark Rift (P. D. Clift, 2015).

The Woodlark Rift example highlights the important contribution of crustal flow during rifting. However, the quantification of crustal flow as well as its dynamic behavior during continental rifting are still poorly understood processes. In particular: how does ductile flow compensate thinning of the upper crust? What is the effect of gradual opening due to rotation (as seen in the Woodlark Rift) on ductile crustal flow and how does a rift-axis parallel flow component (if present) affect the style of rift propagation? And how are brittle near-surface and deep-seated

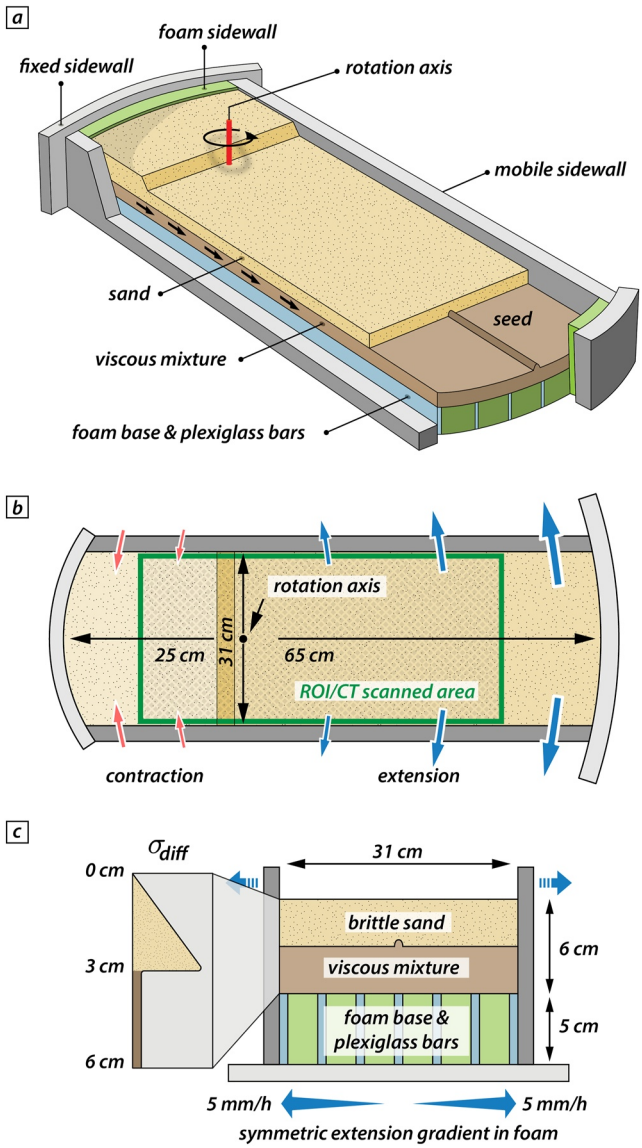


**Figure 2.** Experimental setup for conducted experiments. (a) Cut-out view of the experimental apparatus confined by two curved and fixed, short, and two long movable sidewalls, respectively. The vertical rotation axis separates an extensional from a contractional domain which contains—in certain experiments—an additional sand layer to induce a pressure-gradient driven flow in the viscous layer. (b) Top view of the experimental apparatus and the region of interest (green rectangle). The pivoting motion around the rotation axis causes a divergent velocity gradient with decreasing velocities toward the rotation axis in the extensional domain. In the shortening domain the pivoting motion induces a convergent velocity gradient with decreasing velocities toward the rotation axis. (c) Model set up cross section and schematic strength profile. The two-layer crustal-scale model consists of a brittle sand layer on top of a viscous mixture with a total thickness of 6 cm. To ensure symmetric and homogenously distributed extension, the model sits on top of a foam base, supported by interlayered plexiglass bars, which expands homogeneously after compression prior to the model run.

ductile deformation coupled? To answer these questions, this study presents brittle-ductile 3D analog models of crustal-scale, rotational continental rifting with a particular focus on the role of rift-axis parallel ductile flow. While the previous work of T. C. Schmid, Schreurs, and Adam (2022) analyzed rift propagation and near-surface deformation in detail, this study provides a quantitative analysis of internal deformation. By combining 3D stereo Digital Image Correlation (3D stereo DIC) and Digital Volume Correlation (DVC), we present a novel approach to quantify surface and internal model deformation and gain a comprehensive understanding of crustal flow and its role during rotational continental rifting with an along-strike divergence velocity gradient.

## 2. Methods

We use an experimental apparatus which simulates rotational extension around a pivoting point (Figure 2). An identical setup has been used and described in previous studies of T. C. Schmid, Schreurs, and Adam (2022), Zwaan et al. (2020), and Zwaan and Schreurs (2020). Two short, curved and two mobile long sidewalls confine the model domain (Figure 2a). The mobile sidewalls rotate around a vertical axis which separates the model box into 25 and 65 cm long contractional and extensional model domains, respectively (Figure 2b). The applied maximum divergence velocity is defined along a circular segment at distance 65 cm with respect to the rotation axis. Simultaneously with the opening motion in the extensional domain, shortening occurs in the contractional domain. The initial model surface is defined by a quasi-rectangular area of 90 cm length and 31 cm width. For our analyses, we leave out the curved model parts close to the short sidewalls, resulting in a rectangular area of interest of about 80 by 31 cm. The model overlies a 5 cm thick foam base that is initially compressed and homogenously expands during the experiment runs. This setup allows for a gradually decreasing basal velocity profile with maximum divergence velocity at the mobile sidewalls and zero velocity near the rotational axis (Figure 2c). In the contractional domain, divergence velocities switch polarity and the foam undergoes further contraction. Rigid plexiglass bars sandwiched between the basal foam provide additional support to prevent the overlying model from sinking in. This basal setup has been successfully tested and applied for rotational rift models in T. C. Schmid, Schreurs, and Adam (2022).

The mechanical two-layer model consists of a crustal scale, brittle-viscous setup in which a brittle layer simulates the upper crust and the underlying viscous layer the lower crust (Figure 2c). In the extensional domain, rifting in the brittle layer is localized by applying a viscous seed on top of the viscous layer (Figure 2a). This seed (a semi-cylindrical polydimethylsiloxane [PDMS]/corundum sand mixture rod with radius of ca. 0.5 cm) acts as a pre-existing weak zone along which deformation initiates. We deliberately place the seed along the entire model length to control surface deformation. Note that the absence of a seed results in deformation localization solely along the mobile sidewalls. The applied divergence velocity gradient causes rift propagation toward the rotation axis over time with most mature rift stages developing furthest away from the rotation axis. We place an additional sand layer on top of the contractional domain in some of our models before starting the experiments. This additional gravitational load (see Table 1 for layer

**Table 1**
*Overview of Different Experiments With Varying Brittle-Ductile Thickness Ratio $R_{BD}$ and Additional Gravitational Loading*

| Model name | Brittle layer thickness (cm) | Ductile layer thickness (cm) | Brittle-ductile thickness ratio $T_{BD}$ | Brittle-ductile strength ratio $S_{BD}$ | Additional gravitational loading (cm) | Comment |
|---|---|---|---|---|---|---|
| M2-0 | 4 | 2 | 2 | 117 | 0 | – |
| M2-3 | 4 | 2 | 2 | 117 | 3 | Loading |
| M1-0 | 3 | 3 | 1 | 46 | 0 | – |
| M1-3 | 3 | 3 | 1 | 46 | 3 | Loading |
| M1-0* | 3 | 3 | 1 | 46 | 0 | CT scanned |
| M1-3* | 3 | 3 | 1 | 46 | 3 | CT scanned; loading |
| M1-1* | 3 | 3 | 1 | 46 | 1 | CT scanned; loading |
| M1-0E* | 3 | 3 | 1 | 46 | 0 | CT scanned; ext. only |
| M0.5-0 | 2 | 4 | 0.5 | 17 | 0 | – |
| M0.5-3 | 2 | 4 | 0.5 | 17 | 3 | Loading |

thickness) induces a horizontal pressure gradient and thereby, horizontal flow in the viscous basal layer in the opposite direction of rift propagation (Figures 2 and 3). Prior to the model runs, we sieve a fine 4 by 4 cm grid of corundum sand on the model surface for visual aid and sprinkle coffee powder to create a "salt and pepper" pattern for DIC.

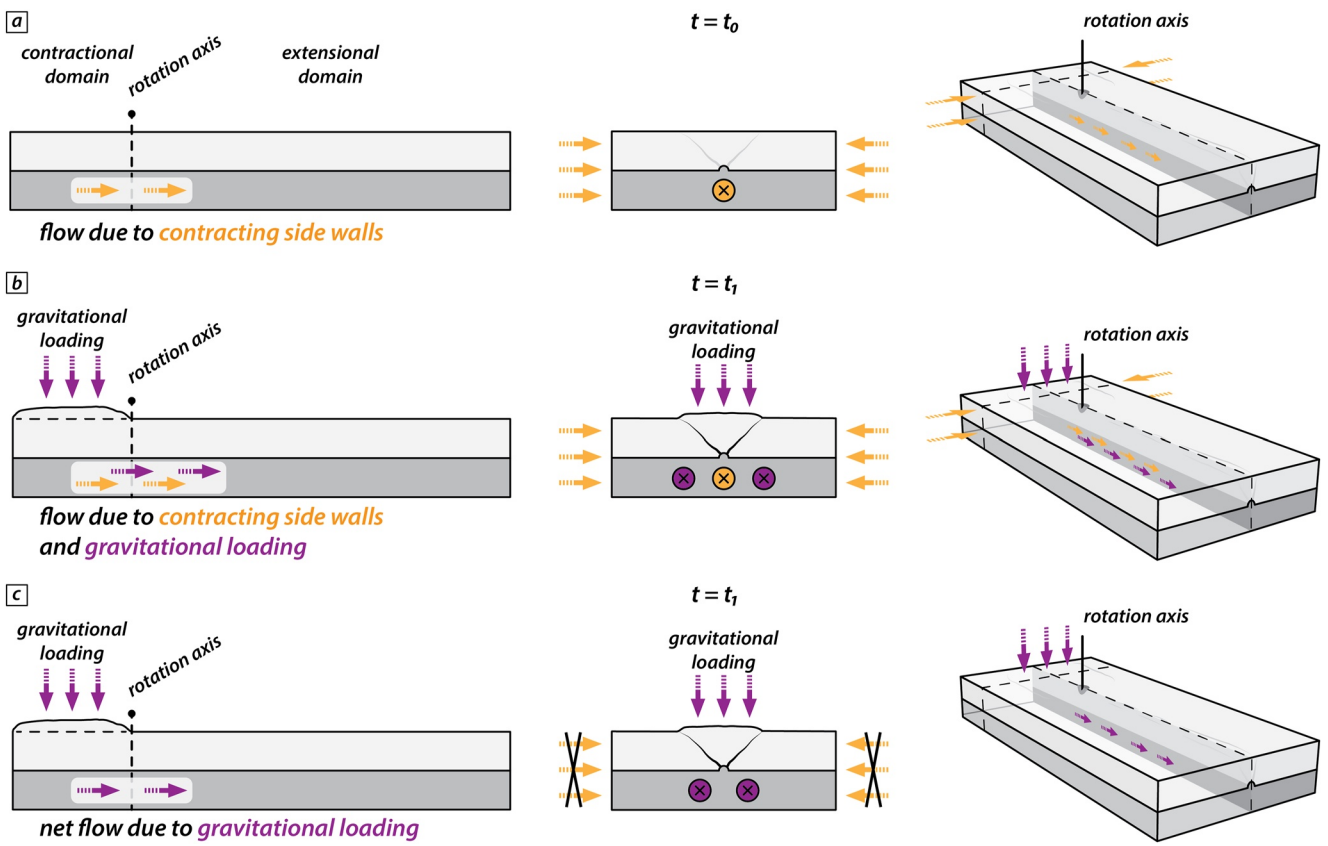


**Figure 3.** Conceptual flow dynamics shown for an experiment with an initial flat model topography. (a) Early stages of model runs prior to deformation localization. Rift-axis parallel flow (longitudinal section) initiates due to contractional side walls (transect) causing a lateral pressure gradient. (b) Ongoing deformation localization causes differential topography due to the formation of a pop-up structure and results in gravitational loading in the contractional domain. This results in an additional rift-axis parallel flow component. (c) The net effect of gravitational loading on rift-axis parallel flow.

**Table 2**
*Material Properties*

| Granular materials | Quartz sand | Corundum sand | Zirshot | Viscous material | PDMS/corundum mixture |
|---|---|---|---|---|---|
| Density (kg/m$^3$) | 1,560* | 1,960* | 2,300 | Density (kg/m$^3$) | 1,600 |
| Grainsize (μm) | 60–250 | 88–175 | 150–210 | Viscosity (Pa s) | $1 \times 10^5$ |
| Peak Friction coefficient $\mu$ and angle | 0.72–36° | 0.78–38° | | Stress exponent n | 1.05 |
| Strain softening (%) | 16 | 18 | | | |
| Cohesion (Pa) | 48 ± 26 | 55 ± 42 | | | |

*Note.* Densities denoted with * are achieved by sieving from 30 cm height.

### 2.1. Analog Model Setup

We conducted a series of crustal scale brittle-viscous analog experiments with variable additional gravitational load-induced pressure gradients causing lateral flow in the viscous layer. For models with an identical brittle-ductile thickness ratio $T_{BD}$ (or identical brittle-ductile strength ratio, $S_{BD}$), we compare the deformation evolution in models with an initially flat model surface (i.e., no additional gravitational load) with corresponding models with an additional gravitational load. This thickness ratio $T_{BD}$ is defined as the brittle layer thickness divided by the viscous layer thickness. The corresponding brittle-ductile strength ratio $S_{BD}$ is listed in Table 1. The overall thickness of the two-layer model was 6 cm for all experiments, representing a 30 km thick, continental crust (McKenzie et al., 2000). However, the thickness ratio $T_{BD}$, between the brittle and ductile layers varies and defines three different model types with $T_{BD}$ = ½, 1, and 2 simulating different crustal configurations. All experiments were run with a maximum divergence velocity of 10 mm/hr (symmetrically 5 mm/hr each side), which linearly decreases toward the rotation axis. This results in a maximum extension of 40 mm or about 13% maximum extension after 4 hr of each model run. Similarly, maximum shortening of 15.4 mm or 5% is reached at the final stage at the distant circular segment in the contractional domain. Lastly, we induced a pressure-gradient driven horizontal flow in the viscous layer by adding an additional quartz sand layer on top of the contractional domain in some models prior to the experiment runs. Thus, the viscous layer flows in the opposite direction to that of rift propagation. For our model naming convention, Mx-y*, the "x" and "y" denotes the brittle-ductile thickness ratio $T_{BD}$ and the height of the additional quartz sand layer on top of the contractional domain, respectively. Models which have been analyzed by XRCT are further denoted with an asterisk. As a reference setup, we use the models M1-x and M1-x* with a brittle-ductile thickness ratio of 1. The complete model series consists of 10 experiments listed in Table 1.

The viscous basal layer consists of a mixture of corundum sand and PDMS with a mixing ratio 1:1 to achieve a density of 1,600 kg/m$^3$. The mixture has a quasi-linear viscosity of $1 \times 10^5$ Pa and a stress exponent of 1.05 (Zwaan, Schreurs, Ritter, et al., 2018). For the upper brittle layer of the analog models, we use dry quartz sand with a bulk density of 1,560 kg/m$^3$ to simulate the upper brittle crust. The desired density is achieved by sieving sand into the model box from a height of 30 cm. The brittle-viscous models thus have a density gradient increasing with depth avoiding density instabilities and spontaneous upwelling of the viscous lower layer. Dilation and localized deformation in the quartz sand locally lowers the peak friction coefficient over time, resulting in strain softening of about 16% (i.e., the difference between the coefficient of peak friction and dynamic friction coefficient normalized by the coefficient of peak friction (Panien et al., 2006) from mutual two-point regression analysispresented in Santimano et al., 2015).

For XRCT scanned experiments, we mix small quantities (weight ratio 1:50) of Zirshot ceramic microbeads with the quartz and corundum sands which enhances volumetric patterns in CT scans to facilitate DVC analysis (Adam et al., 2013). Additionally, we sieve a thin layer of corundum sand from 30 cm height on top of the viscous mixture before adding quartz sand to enhance the X-ray absorption contrast between the viscous and brittle domains. The influence of the ceramic microbeads and the thin corundum sand layer on the overall mechanical properties is negligible (Klinkmüller, 2011; Panien et al., 2006; T. Schmid et al., 2020a, 2020b) 2020a. All material properties are listed in Table 2.

**Table 3**
*Scaling Parameters and Scaling Ratios for the Reference Model Setup With a Brittle Ductile Thickness Ratio $T_{BD} = 1$*

| | General parameters | | | Brittle upper crust | | Ductile lower crust | | Dimensionless numbers | | |
|---|---|---|---|---|---|---|---|---|---|---|
| | Gravity ($m/s^2$) | Crustal thickness (m) | Extension velocity (m/s) | Density ($kg/m^3$) | Cohesion (Pa) | Density ($kg/m^3$) | Viscosity (Pa s) | Smoluchowski $S_m$ | Ramberg $R_m$ [a] | Reynolds $R_e$ |
| Model | 9.81 | $6 \times 10^{-2}$ | $2.8 \times 10^{-6}$ | 1,560 | 50 | 1,600 | $1 \times 10^5$ | 1 | 34 | <<1 |
| Nature | 9.81 | $3 \times 10^4$ | $1.4 \times 10^{-10}$ | 2,700 | $5 \times 10^7$ | 2,900 | $5 \times 10^{20}$ | 1 | 36 | <<1 |
| Scaling ratios $x^* = x^m/x^n$ (dimensionless) | | | | | | | | | | |
| | $\sigma^*$ | $\rho^*$ | $g^*$ | $h^*$ | $c^*$ | $\dot{\epsilon}^*$ | $\eta^*$ | $v^*$ | $t^*$ | |
| | $1 \times 10^{-6}$ | 0.55 | 1 | $2 \times 10^{-6}$ | $1 \times 10^{-6}$ | $6 \times 10^9$ | $2 \times 10^{-16}$ | $1 \times 10^4$ | $2 \times 10^{-10}$ | |

[a]Note that for calculating $R_m$ the maximum velocity is used.

### 2.2. Scaling

We apply standard scaling equations from Hubbert (1937) and Ramberg (1981) to ensure proper scaling of our models with respect to nature. For brittle Mohr-Coulomb type materials and viscous materials, dynamic similarity is given by the stress ratio $\sigma^* = \rho^* g^* h^*$, and strain-rate ratio $\dot{\epsilon}^* = \sigma^*/\eta^*$, respectively.

By convention, $\sigma^*$ is defined as: $\sigma^* = \sigma_m/\sigma_n$, where subscripts $m$ and $n$ indicate values for the model and nature, respectively. Further, $\rho^*$, $g^*$, $h^*$, and $\eta^*$ are the density, gravity, length, and viscosity scale ratios, respectively. In our models, 1 cm represents 5 km in nature which yields a length scaling factor of $h^* = 2 \times 10^{-6}$. The stress and density scaling ratios are approximately $\sigma^* = 1.2 \times 10^{-6}$ and $\rho^* = 0.6$, respectively. The cohesion of quartz sand is about 60 Pa and upper crustal rocks are about 50 MPa (Byerlee, 1978), giving a cohesion scaling ratio $c^* = 1.2 \times 10^{-6}$.

Assuming a lower crustal viscosity of $\eta = 5 \times 10^{20}$ Pa s (e.g., Kruse et al., 1991) yields a viscosity scaling ratio $\eta^* = 2 \times 10^{-16}$ and a strain rate scaling ratio $\dot{\epsilon}^* = 6 \times 10^9$. Further, the velocity $v^*$ and time $t^*$ scaling ratios are calculated from $\dot{\epsilon}^* = v^*/h^* = 1/t^*$, yielding a velocity scaling ratio $v^* = 1.2 \times 10^4$ and time scaling ratio $t^* = 2 \times 10^{-10}$. Hence, 1 hr in our analog experiments translates to about 0.66 Ma in nature and the applied extension velocity (10 mm $hr^{-1}$) refers to a velocity of 8 mm $a^{-1}$ and strain-rate values of $8 \times 10^{-15}$ $s^{-1}$ in nature.

We ensure dynamic and kinematic similarity between nature and the experiments by calculating the Smoluchowski number $S_m$, and the Ramberg number $R_m$ for the brittle and viscous layers, respectively. $S_m$ is defined as the ratio between gravitational stress and cohesive strength (Ramberg, 1981) $S_m = \rho g h/(C + \mu \rho g h)$, where $\rho$, $h$, $C$, and $\mu$ are the density, thickness, cohesion and friction coefficient, respectively. Since upper crustal rocks have a cohesion values of 50 MPa and internal friction coefficients of ~0.6 (Byerlee, 1978), this yields $S_m$ ~1 for both our experiments and nature. For our reference model setup with a brittle-ductile thickness ratio $T_{BD} = 1$, the Ramberg number $R_m = \rho g h^2/\eta v$ yields values of 51 and 53 for our experiments and nature, respectively. For models with $T_{BD} = 2$, $R_m$ values are 23 and 24 for the experiments and nature, respectively. For models with $T_{BD} = 0.5$, $R_m$ ~90 and ~95 for the experiments and nature, respectively. The Reynolds number $R_e = \rho v h/\eta$ is defined as the ratio between inertial forces and viscous forces and is <<1 for all of our experiments and nature.

Based on the above scaling laws, the material properties and similar non-dimensional numbers for the models and nature, we consider our analog experiments to be properly scaled. Model parameters and non-dimensional numbers are given in Table 3.

### 2.3. Contractional Boundary Condition and Induced Pressure Gradient

During opening of the extensional domain of the apparatus, shortening in the contractional domain induces a lateral pressure gradient, resulting in rift-axis parallel flow of the lower viscous layer from the contractional to the extensional model domain (Figure 3a). With subsequent deformation localization in the contractional domain, differential topography increases the lateral pressure gradient, enhancing rift-axis parallel flow (Figure 3b). Additionally, we simulate different additional gravitational loadings by using sand layers of 1 and 3 cm on top of the

contractional model domain. To analyze the net effect of such additional gravitational load on the rift-axis parallel flow in the lower viscous layer, the flow component induced by contracting the sidewalls must be subtracted from the total flow. However, in our models the contribution of the contracting sidewalls is negligible.

Based on the above scaling relationships, a 3 cm thick additional sand layer translates to 15 km in nature, which exceeds realistic elevation values. However, we use such an exaggerated gravitational load to enhance and visualize the displacement dynamics, which are present in all our models, even without an additional gravitational load (Figure 3). The additional sand load causes a pressure gradient from the contractional to the extensional model domain, which drives rift-parallel flow in the viscous layer. If the relative displacement between the bounding layers (i.e., foam base and overlying sand layer) is zero, such a pressure-gradient driven flow is known as Poiseuille flow and its analytical 1D solution is given by:

$$u(z) = \frac{1}{2\mu}\frac{dp}{dx}\left(z^2 - hz\right) \tag{1}$$

(e.g., Turcotte & Schubert, 1982). Here, $u(z)$ denotes the lateral flow velocity at the vertical position $z$ in a channel with height $h$. Further, $\mu$ is the viscosity of the fluid in the channel and $dp/dx$ the lateral pressure gradient along the horizontal length of the channel. In some of our experiments, we induce a lateral pressure gradient by an initial topographic elevation with pressure $p_{topo}$ given by

$$p_{\text{topo}} = \rho_s \times g \times T(x) \tag{2}$$

(Clark & Royden, 2000), where $\rho_s$ is the density of the additional brittle sand layer (1,560 kg/m$^3$), and $g$, and $T(x)$ are the gravitational acceleration and topographic elevation along the model length $x$, respectively. To measure the net horizontal flow due to the pressure gradient (Figure 3c), we XRCT scan a model with initially flat topography (M1-0*) and quantify the flow velocity due to contracting sidewalls (Figure 3a). Note that the flow velocity is diverging and decreases toward the extensional far end. Along the moving sidewalls the flow velocity is zero due to friction (i.e., no-slip boundary condition).

### 2.4. Deformation Monitoring

We use an automated light and camera setup to monitor surface deformation by means of top view images for qualitative description as well as sets of stereo images for further 3D displacement analysis using 3D stereoscopic DIC (Adam et al., 2005). For the qualitative surface evolution description, we use a Nikon D200 (10.2 Mpx) DSLR camera mounted above the experiment apparatus. Two Nikon D810 (36 Mpx) DSLR cameras are aligned on a horizontal bar above the model surface with an angle of ca. 30° with respect to each other providing a setup for stereoscopic images and subsequent 3D DIC analysis.

For imaging the internal model deformation, we run models with a reference thickness ratio $T_{\text{BD}} = 1$, that is, a 3 cm thick sand layer overlying a 3 cm thick viscous layer, with initial flat topography (M1-0*), and models with additional quartz sand layers of 1 cm (M1-1*), and 3 cm (M1-3*) on top of the contractional domain in a medical XRCT scanner (64 slice Siemens Somatom Definition AS X-ray CT-scanner). The models are scanned with a 20-min interval (corresponding to 3.3 mm divergence or 1% maximum extension). Additionally, we scanned an experiment with $T_{\text{BD}} = 1$ with no material (i.e., upper, and lower crust and additional sand layer) placed on the compressional part of the apparatus (M1-0E*). The resolution of the scans is 512 by 512 pixels for each slice with a size of 37 by 37 cm (~0.72 by 0.72 mm/px). For every time step, models must be halted and scanned three times for quantitative DVC. Each individual scan has a duration of ca. 1 min with a time gap of ca. 30 s between the three scans. The CT scanner required such cool-down periods which were kept at a minimum by reducing the horizontal scan area (68 by 31 cm; Figure 2b) to avoid ongoing deformation in the time-dependent viscous layer.

### 2.5. Data Analysis and Post Processing

For the quantitative analysis of surface deformation, we use the StrainMaster module from the commercial DaVis image correlation software (Ver. 8.4, LaVision). Since image correlation yields time-series incremental

displacement fields on a fixed Eulerian grid, we use Lagrangian summation, to obtain finite deformation. Based on displacement fields, the infinitesimal strain tensor $E$ is obtained from:

$$E_{ij} = \frac{\partial v_i}{\partial x_j} \tag{3}$$

with the following components in 2D:

$$E = \begin{bmatrix} E_{xx} & E_{xy} \\ E_{yx} & E_{yy} \end{bmatrix}. \tag{4}$$

$E_{xx}$ and $E_{yy}$ are the normal strain components in $x$ and $y$ directions, respectively and $E_{xy}$ and $E_{yx}$ are the shear strain components. The maximum principal stretching axis (largest eigenvalue of the strain tensor) defines the magnitude of the maximum normal strain, $E_{\max}$, where:

$$E_{\max} = \frac{(E_{xx} + E_{yy})}{2} + \sqrt{\left| \frac{(E_{xx} - E_{yy})^2}{4} + \frac{(E_{xy} + E_{yx})^2}{4} \right|}. \tag{5}$$

Since $E_{\max}$ is invariant to the coordinate system, we use it to describe deformation in our experiments where rigid body rotation occurs around a fixed axis.

Unlike cutting wetted analog models at their final stage, CT scanning provides a non-destructive manner to gain insights into transient internal deformation during experiment runs. As in our surface strain analysis, we use commercial DaVis software (Version 10.2, LaVision) for quantifying internal 3D deformation captured in CT scan images. The DVC module of this software computes 3D displacement fields by cross correlating intensity patterns from subsequent volumetric (CT scanned) data sets collected over time (Adam et al., 2013; Poppe et al., 2019; Zwaan, Schreurs, & Adam, 2018). The data volume is divided into smaller voxel sub-volumes to determine local displacement vectors by identifying similar intensity patterns in subsequent volume data sets. In contrast to 2D correlation, peaks are represented by a spherical blob in 3D and for each sub-volume the best matching position is associated with displacement vector components $dx$, $dy$, and $dz$ from the initial to the deformed volume. As each sub-volume yields only one displacement vector, spatial vector resolution is increased by placing sub-volumes next to each other at a distance $d$, smaller than the voxel edge length $L$ to create a sub-volume overlap. Making use of a multi-pass cross correlation, DaVis first applies a computationally efficient Fast Fourier Transform (FFT) algorithm for coarse sub-volumes to predict displacement fields for subsequent iterations which are done using a direct correlation (DC) algorithm.

Using the smallest XRCT slice thickness of 0.6 mm/px the volumetric data consists of voxels with dimensions of 0.72 by 0.72 by 0.6 mm/px. Since DVC requires cubic voxels with the same edge length along all three axes, the images must be re-processed before conducting quantitative analysis. In our anisotropic voxels the $y$ axis (slice thickness of 0.6 mm/px) provides the best resolution in the volumetric data set, and we adjust pixel sizes (0.72 mm by 0.72 mm) in the $xz$-plane to obtain isotropic 0.6 mm sided voxels. We apply a nearest neighbor resampling algorithm in ImageJ to increase the pixel number in the $xz$-plane (Figure 4) without creating artificial pixel intensity values due to interpolation. As the models are scanned multiple times per time step, we further stack the voxel data to increase intensity values. In addition, this step reduces noise created by the high X-ray reflectivity Zirshot ceramic beads and improves the image quality. For DVC analyses, we use sub-volume sizes of 128 pixels with an overlap of 50% for the first step (FFT). Further iterations (DC) subsequently decrease sub-volume sizes to 64, 32 and 16 pixels with overlaps of 50% and 75% for the final step. Where sub-pixel displacements are not captured by the discrete correlation peak, fitting of a Gaussian curve restores accuracy. The final sub-volume displacement vectors are assembled to construct incremental (here dt = 20 min) 3D displacement fields. Incremental displacements are in the order of 1–2 mm for all three displacement components with an uncertainty of 0.03 and 0.06 mm in planes parallel and normal to the CT scan slices, respectively.

Processing of 3D DIC data follows the protocol of T. C. Schmid, Schreurs, and Adam (2022). Like DIC data, we process data from DVC analyses in MATLAB (Version 18b) and Python (Version 3.7) to quantify deformation. For volumetric visualization we use Tecplot360 (Version 2018) software. A more detailed overview of DIC and DVC parameters can be found in T. Schmid et al. (2021) and T. C. Schmid, Rudolf, et al. (2022), respectively.

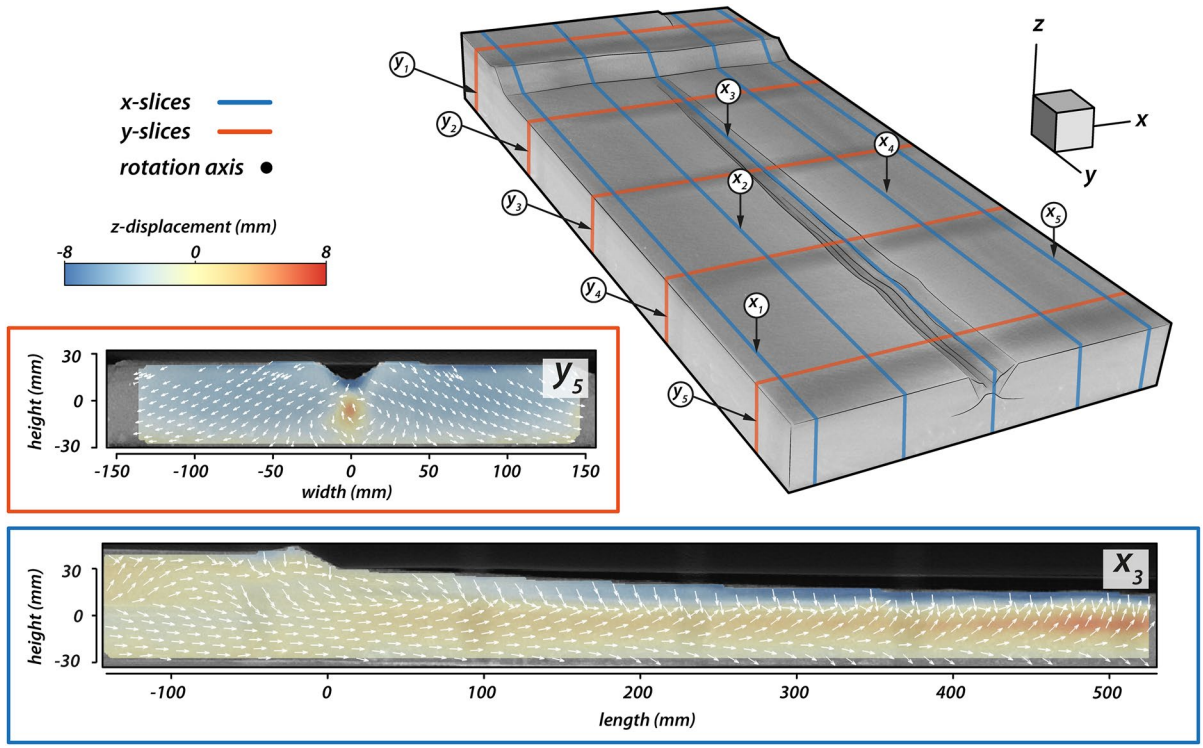


**Figure 4.** Positions of all extracted 2D slices from Digital Volume Correlation analyses. *X* slices refer to vertical, longitudinal transects. *Y* slices refer to cross section transects. As an example, in both slices the colors refer to the vertical displacement component *Dz* and white arrows indicate the total displacement, projected into the plane. All transects, including horizontal *z* slices can be found in an additional data publication on the GFZ data repository (T. C. Schmid, Rudolf, et al., 2022).

## 3. Results

The complete model series consists of 10 experiments (see Table 1). Before quantifying surface deformation, we describe the first-order evolution based on top view images and CT scans, to provide qualitative insights into the deformation evolution. First-order deformation features such as rift propagation show strong similarities in all models. Hence, we use a model with the reference brittle-ductile thickness ratio $T_{BD} = 1$ and an additional sand layer of 3 cm on top of the contractional domain, to describe the overall deformation evolution. Note, that an identical setup with an initially flat topography has been previously described in Zwaan et al. (2020) and T. C. Schmid, Schreurs, and Adam (2022).

### 3.1. General Rift Evolution for Models With Gravitational Load

Differences in strain evolution among models with or without additional gravitational load, and with varying brittle-ductile ratios are inconspicuous and hence, difficult to assess. This highlights the necessity to further analyze deformation quantitatively. However, we briefly describe characteristic stages of rift evolution under the influence of an additional gravitational load. Figure 5 shows the rift evolution in model M1-3*. After 3.3 mm of maximum extension (i.e., 20 min), a set of conjugate dip-slip faults forms, expressed by short segments at the surface 400–600 mm away from the rotation axis (Figures 5a, 5d and 5g). While this is difficult to distinguish in top views (Figure 5a), XRCT scans of the corresponding transect (Figure 5d) clearly depict a set of conjugate normal faults with a dip angle of about 70° (Figure 5g). With increasing bulk extension, these conjugate normal faults propagate toward the rotation axis, forming a continuous rift structure delimited by rift boundary faults. After 23.1 mm of maximum extension (i.e., 140 min; Figures 5b, 5e and 5h), the rift boundary faults have gently rotated about a horizontal axis to a dip angle of about 64° (Figure 5h). Simultaneously, a new set of conjugate normal faults forms in between the rift boundary faults (intra-rift faults). Like the rift boundary faults, the intra-rift faults initially form as isolated segments within the rift (Figures 5b and 5e). At the final stage (i.e., 40 mm maximum extension and 240 min; Figures 5c, 5f, 5i and 5j), the rift boundary faults have propagated as far

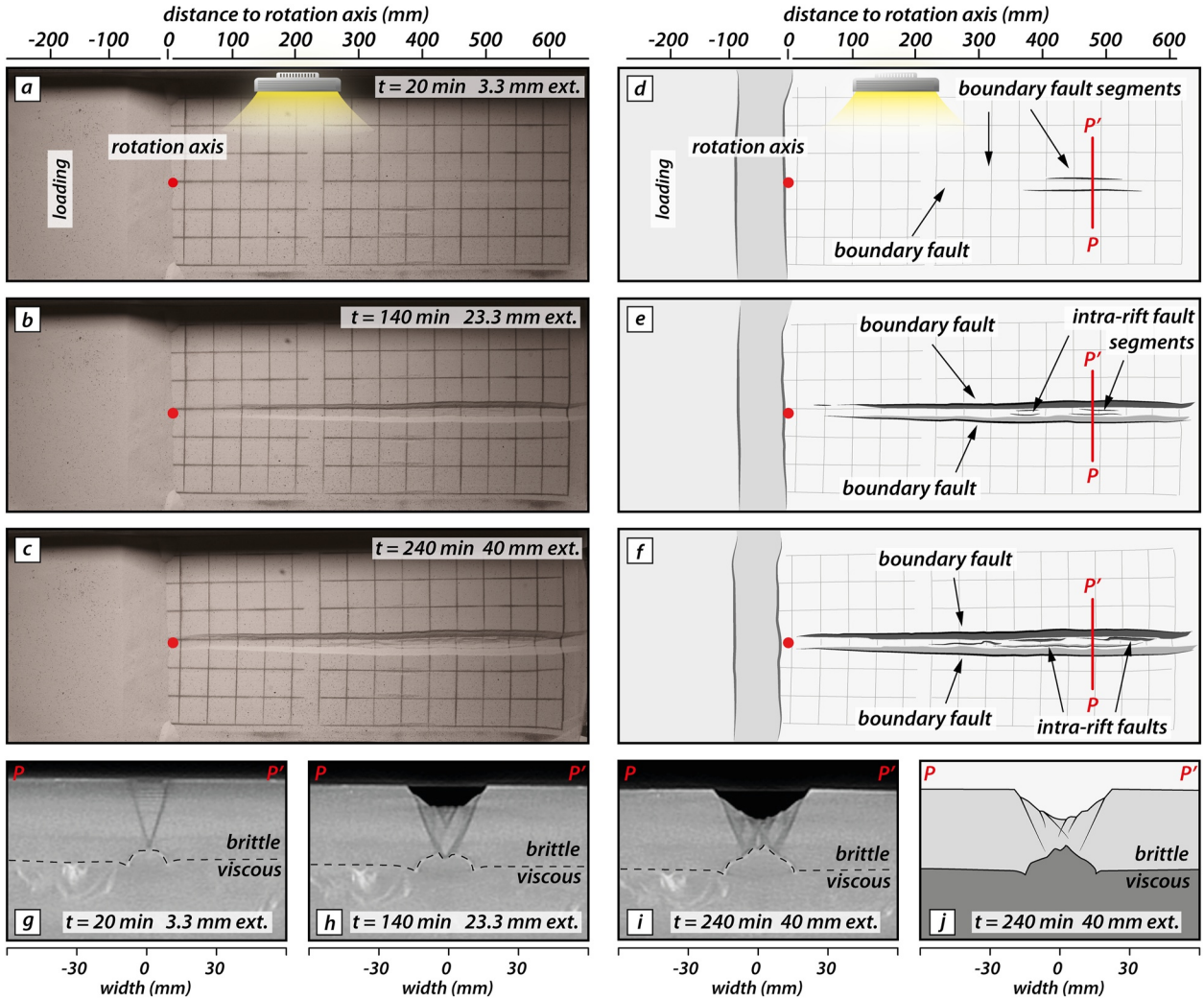


**Figure 5.** Surface evolution of model M1-3* and pertinent CT cross sections at positions indicated by red profiles P–P′. (a–c) Top view images of selected model stages after 20, 140, and 240 min. (d–f) Key features of the rift evolution at corresponding time steps with respect to top view images. (g–i) XRCT image slices at positions indicated by red profile lines. (j) Sketch of corresponding XRCT slice at the final model stage (i). Initial rift structures are visible after 20 min and ca. 3 mm extension (a, d, g) indicated by a short segment of two conjugate normal faults forming rift boundary faults. Rift boundary faults propagate toward the rotation axis forming a continuous rift structure with intra-rift fault segments forming at around 140 min and ca 23 mm maximum extension (b, e, h). At the final stage rift boundary faults fully propagated toward the rotation axis and formerly isolated intra-rift segments partially linked into longer, continuous segments propagating toward the rotation axis (c–j).

as the rotation axis, where bulk extension is zero (Figures 5c and 5f). Formerly isolated intra-rift fault segments have partially connected and consist of longer fault segments propagating toward the rotation axis.

The intra-rift faults show a less advanced stage of propagation when compared to models with an identical crustal configuration but flat topography (e.g., M1-0*; T. C. Schmid, Schreurs, & Adam, 2022). Figure 6 compares rift morphologies of models M1-0* and M1-3* at the final stage. The rift morphology in model M1-0* shows three distinct pairs of conjugate normal faults with successively younger faults toward the rift center (Figures 6a, 6b and 6d). Each fault generation bounds a graben structure resulting in increasing subsidence toward the rift center. In contrast, rifting in model M1-3* shows a less advanced stage with only two generations of conjugate normal faults present (Figures 6e, 6f and 6h). Note that thrusting in the contractional domain is entirely suppressed in model M1-3*. XRCT scan imagery from the corresponding cross section reveals that the gravitational load entirely inhibits thrust development (Figures 6c and 6g).

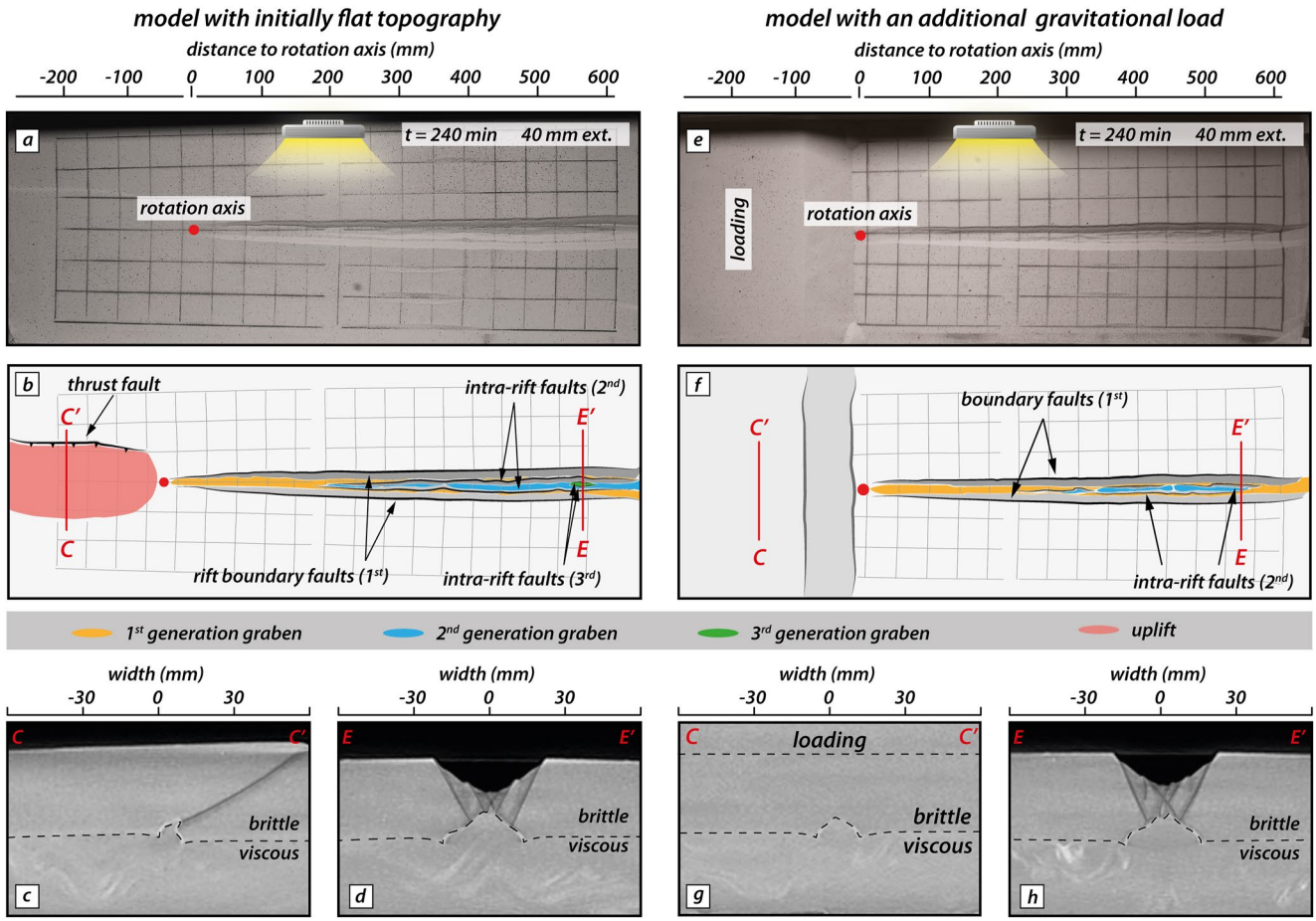


**Figure 6.** Comparison of the final state of a model with initially flat topography (M1-0*; (a–d)) and a model with an additional gravitational load of 3 cm (M1-3*; (e–h)). Red lines C′–C and E′–E indicate positions of XRCT cross sections in the contractional and extensional domain, respectively. Note that model M1-3* shows a less advanced internal rift evolution at the final stage.

### 3.1.1. Propagation of Rift Boundary Faults

We investigate lateral rift propagation by tracking the position of the rift boundary fault tips with respect to the rotation axis over time. For this, we set a threshold of 10% of cumulative surface strain identical to T. C. Schmid, Schreurs, and Adam (2022). Figure 7 shows the mean rift tip position (i.e., the mean position of the two conjugate rift boundary faults) for all 10 experiments. For all models, rift propagation follows a distinct trend with rapid rift lengthening in an early stage and slower propagation in a second stage. All models show onset of rift propagation at around 1.3% of maximum extension. However, rift onset in models with an initially flat topography tends to occur earlier compared to models with gravitational loading. For models with a brittle-ductile thickness ratio $T_{BD} = 2$, the mean rift propagation path is nearly identical but with a decreasing brittle-ductile ratio, the onset of rift propagation is successively retarded for models with a gravitational load.

### 3.1.2. Inward Migration of Fault Activity

The delayed rift propagation in experiments with gravitational loading is clearly visible in surface strain-rate maps obtained from DIC analysis (Figure 8) which we use as a proxy for fault activity. T. C. Schmid, Schreurs, and Adam (2022) document three generations of conjugate normal faults for a brittle-ductile thickness ratio $T_{BD} = 1$. For an initial flat topography (M1-0*; Figures 8a–8c), fault activity progressively abandons rift boundary faults and migrates inwards onto intra-rift faults. After about 23 mm of maximum extension, strain-rate values decrease along boundary fault segments that are further away from the rotation axis. Simultaneously, fault activity migrates inward onto conjugate intra-rift normal faults. At the final stage (i.e., after 40 mm of maximum extension), three different fault generations are active in different rift segments with increasing bulk strain along

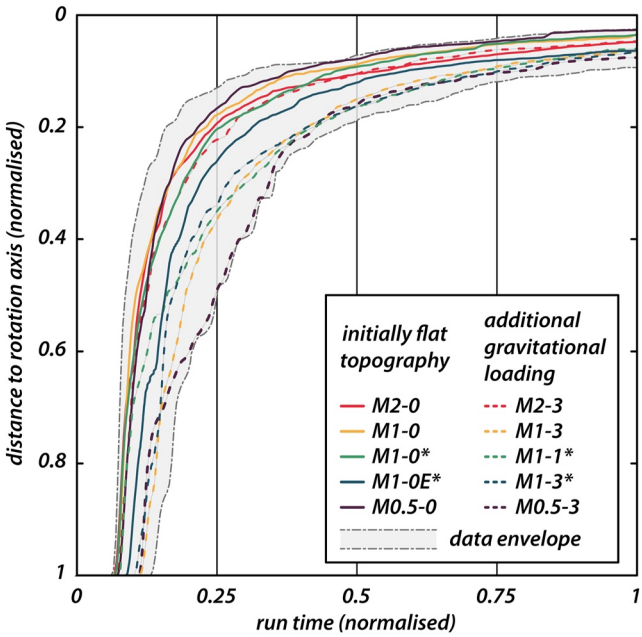


**Figure 7.** Normalized rift propagation and growth of rift boundary faults for all 10 experiments. Each line tracks the mean rift tip (i.e., the mean position of the two conjugate rift boundary faults) position over time, whereas the envelope depicts the range of all individual rift boundary faults. Solid lines correspond to models with different brittle-ductile thickness ratios, $T_{BD}$, but initial flat topography. Dashed lines correspond to models with different $T_{BD}$ and an additional gravitational load of either 1 or 3 cm. Note that a decreasing $T_{BD}$ leads to subsequent rift propagation delay in models with an additional gravitational load but has no effect on models with initial flat topography.

the rift axis. In model M1-3* (Figures 8d–8f) with an additional gravitational load, early stages (e.g., at 20 min; Figures 8a and 8d) show similar strain-rate patterns along rift boundary faults compared to model M1-0*. However, the onset of inward migration is delayed for model M1-3*. After about 23 mm of maximum extension, inward migration initializes fault activity along intra-rift faults (Figure 8e) whereas in model M1-0* intra-rift faults consist of longer segments in the distal model part (Figure 8b). In contrast to model M1-0* only two generations of conjugate fault pairs are active at the final stage (Figure 8f) indicating a less advanced rift maturity for model M1-3*. Presumably, the rift structure in model M1-3* will become as mature as that in model M1-0* at a later time.

### 3.2. Vertical Surface Motions

The cumulative vertical displacement, $Dz$ (Figure 9), is used to compare the surface topography in the final stage of all experiments with an additional gravitational load (Mx-3 and Mx-1) with the corresponding experiments with an initially flat topography (Mx-0). Note that these motions only indicate net uplift and subsidence and do not necessarily represent the absolute topography. The cumulative horizontal displacement vector field is also indicated in Figure 9 by gray arrows (not to scale) as a visual aid. Regardless of the brittle-ductile thickness ratio, $T_{BD}$, the final topography of models with an initially flat topography (Figures 9a–9e) are nearly identical, with maximum subsidence values in the rift structure occurring at distances far away from the rotation axis. For $T_{BD}$ = 2, 1, and 0.5, maximum subsidence values are about −20, −15, and −10 mm, respectively. Maximum uplift values occur in the contractional domain (except model M1-0E*; Figure 9d) and are in the order of about 5 mm for all models with an initially flat topography. The zero-elevation line (black line) separates zones of uplift and subsidence which, in the case of initially flat topography models, coincides with domains separating contraction from extension. Note that the extensional domain shows patterns of diffuse subsidence outside the rift. This regional subsidence is due to the homogeneous thinning of the lower viscous layer, which is placed on top of rigid basal setup that does not allow isostatic compensation. The maximum rift and pop-up structure width depends on the absolute thickness of the brittle layer. Maximum subsidence values decrease with lower $T_{BD}$ ratio.

In models with an additional gravitational load (Figures 9f–9j), parts of the extensional domain, that are located farther away from the rotation axis show identical subsidence patterns when compared to models with identical $T_{BD}$ but an initially flat topography. However, experiments with an additional gravitational load show enhanced vertical motions in model parts closer to the rotation axis in both the contractional and extensional domain. For models with $T_{BD}$ = 2, the zone of uplift in model M2-3 (Figure 9f) shrinks (in contrast to model M2-0; Figure 9a), as the zero-elevation contour migrates into the compressional domain. Absolute maximum uplift values are of the same order of magnitude, however, the rift tip in the extensional domain is flanked by zones of minor net uplift in model M2-3 (Figure 9f) compared to model M2-0 (Figure 9a). Models with $T_{DB}$ = 1 and an additional gravitational load of 3 cm (M1-3 and M1-3*; Figures 9g and 9h) show a clear distinction between a zone of maximum subsidence of −2 mm in the contractional domain (i.e., location of the additional gravitational load) and a bulge-like uplift zone with maximum values of 2 mm at the transition from contraction to extension. The rift is not influenced by this uplift as it propagates toward the rotation axis and through the bulge, resulting in uplifted flanks on either side of the propagating rift. In model M1-1 (Figure 9i) with $T_{BD}$ = 1, the additional gravitational load is reduced to a sand layer with a thickness of 1 cm. Identical to models M1-3 and M1-3*, a zone of subsidence develops in the contractional domain. However, maximum subsidence values do not exceed 1 mm and do not overprint net uplift in the contractional domain farther away from the rotation axis where thrusting persists. The adjacent uplifted bulge in the extensional domain is only minor with values <1 mm. The effect of the gravitational load is most pronounced in model M0.5-3 with $T_{BD}$ = 0.5. Here, subsidence values within the contractional domain are largest and reach −7 mm. The surface of the contractional domain subsides homogeneously

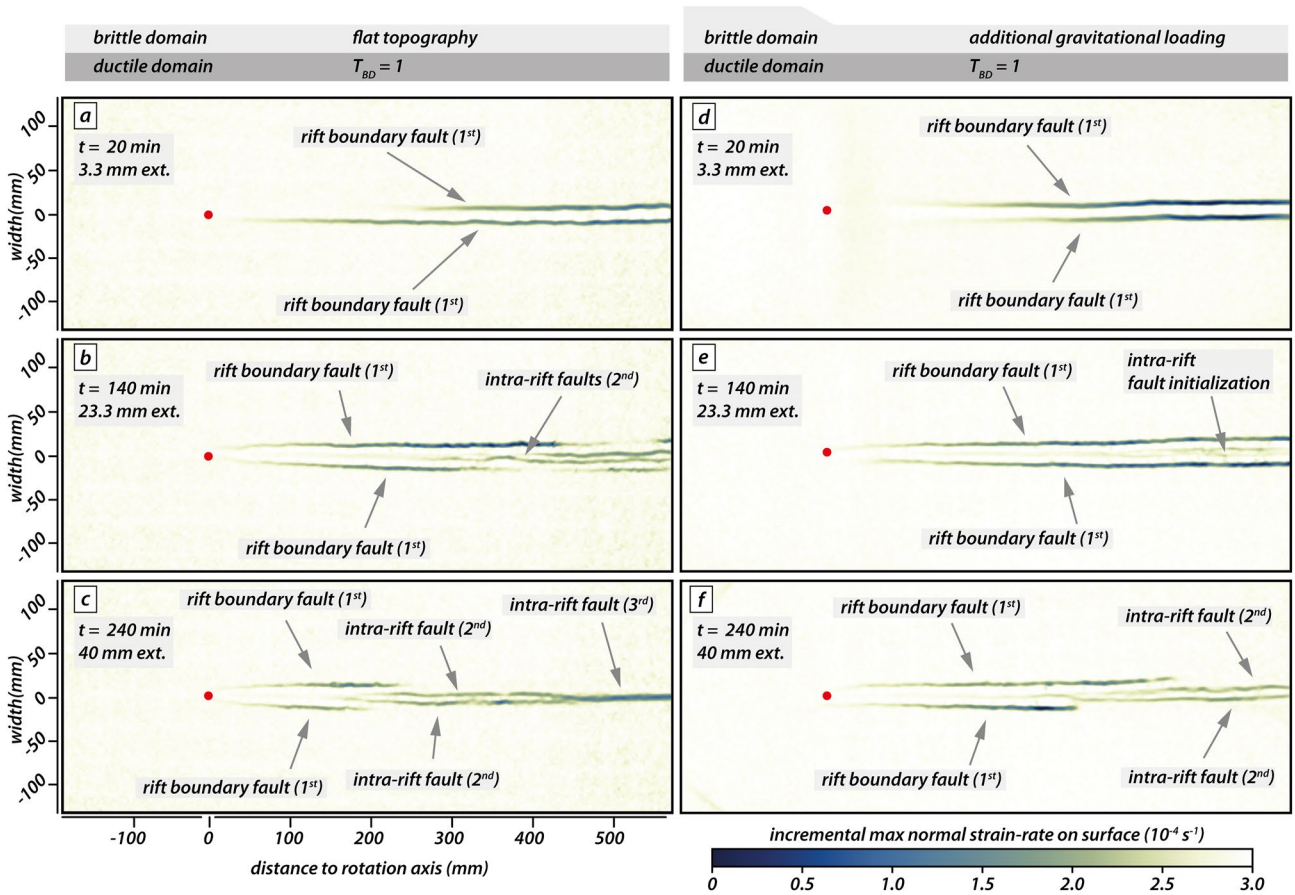


**Figure 8.** Comparison of strain rate maps of a model with initially flat topography (M1-0*; (a–c)) and a model with an additional gravitational load of 3 cm (M1-3*; (d–f)) for different time steps. Strain rates in model with flat topography show progressive abandonment of rift boundary faults and rift inward migration of faulting activity (a–c). In contrast, in the model with an additional gravitational load, inward migration of fault activity occurs later during the experiment run, resulting in a longer and more pronounced fault activity along rift boundary faults (d–f). Incremental maximum normal strain rate refers to Equation 5 divided by $\Delta t = 60$s.

and has a sharp boundary to the adjacent uplift bulge, where maximum uplift values are around 5 mm. The uplift bulge continues far into the extensional domain and eventually uplift is large enough to suppress net subsidence in the rift near the rotation axis (Figure 9j). Note that the horizontal vector field in models with an additional gravitational load deviates increasingly from the reference state (i.e., models with initial flat topography) as $T_{BD}$ decreases.

### 3.3. Internal Deformation Analysis

We now focus on quantification of the internal deformation in XRCT scanned models with an intermediate brittle-ductile thickness ratio $T_{BD} = 1$ (M1-0E*, M1-0*, M1-1*, and M1-3*). Specifically, we analyze the flow field in the viscous domain by means of cumulative displacement vector fields and focus on the horizontal component of rift-parallel flow (i.e., along the model $y$-axis). Figure 4 gives an overview of the data slices extracted from DVC analyses of all four XRCT scanned models. For each model, we extract individual 3D displacement components on five $x$-slices (i.e., $yz$-planes; $x_1 - x_5$) and five $y$-slices (i.e., $xz$-planes; $y_1 - y_5$). Additionally, we extract displacement vectors from horizontal $z$-slices in both the brittle and viscous domains (i.e., $xy$-planes; $z_1$ and $z_2$). For all slices, the displacement vectors represent the total 3D displacement, projected into the plane of the corresponding CT slice. The entire slice compilation is available in an additional data publication (T. C. Schmid, Rudolf, et al., 2022). Here, we present a representative selection of displacement data to document quantitative 3D deformation features in our XRCT-scanned models.

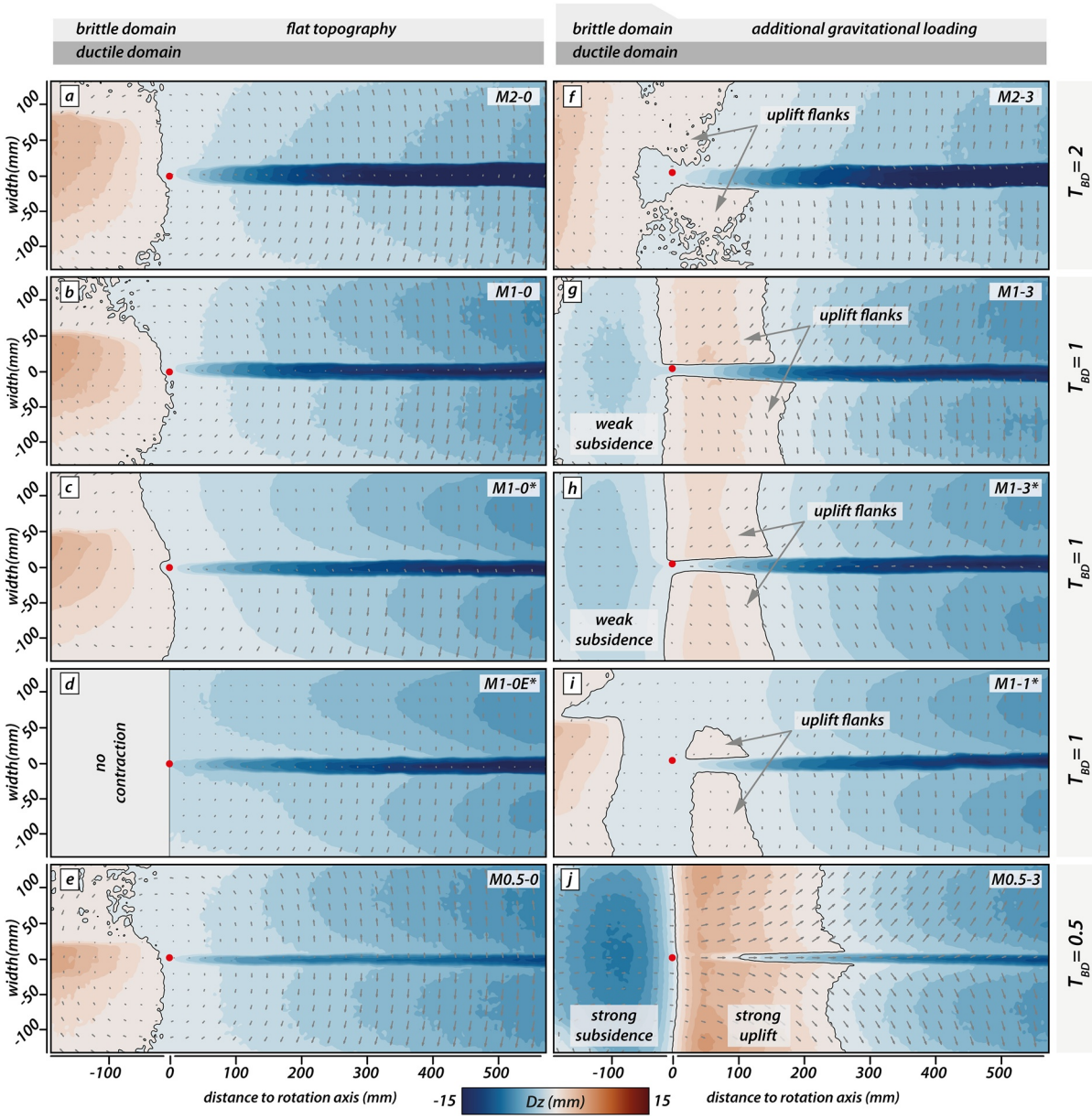


**Figure 9.** Cumulative vertical displacement maps at the final model stage. (a–f) Models with different brittle-ductile thickness ratio $T_{BD}$ and an initial flat topography. (f–j) respective models with an additional gravitational load (M2-3, M1-3, M1-3*, and M0.5-3: 3 cm; M1-1*: 1 cm). For all models with an initial flat topography, final surface expressions are identical with small variations in absolute subsidence values. Surface expressions in models including an additional gravitational load deviate from the pertinent flat topography models. Black lines indicate zero-elevation. Gray arrows indicate the horizontal displacement field.

### 3.3.1. Displacement Components in Vertical Rift Perpendicular Transects $y_1$ and $y_5$

Apart from differences in the absolute values of displacements, similar observations are made in the *y*-slices of all XRCT scanned models. Therefore, we only show the $y_1$ and $y_5$ slices of model M1-0* in Figure 10, which plots the horizontal displacement components *Dx* (a and d) and *Dy* (b and e), and the vertical displacement *Dz* (c and f) at the final stage after 4 hr of the model run (i.e., 40 mm max. extension). In addition, white arrows indicate the 3D displacement projected into the plane. The left column shows displacement components in position $y_1$, in the contractional domain, whereas the right column shows displacement components in position $y_5$ at the far end of the extensional domain. Values of the cumulative horizontal displacement components *Dx*, *Dy*, and *Dz* range from −15 to 15, −5 to 5, and −8 to 8 mm, respectively.

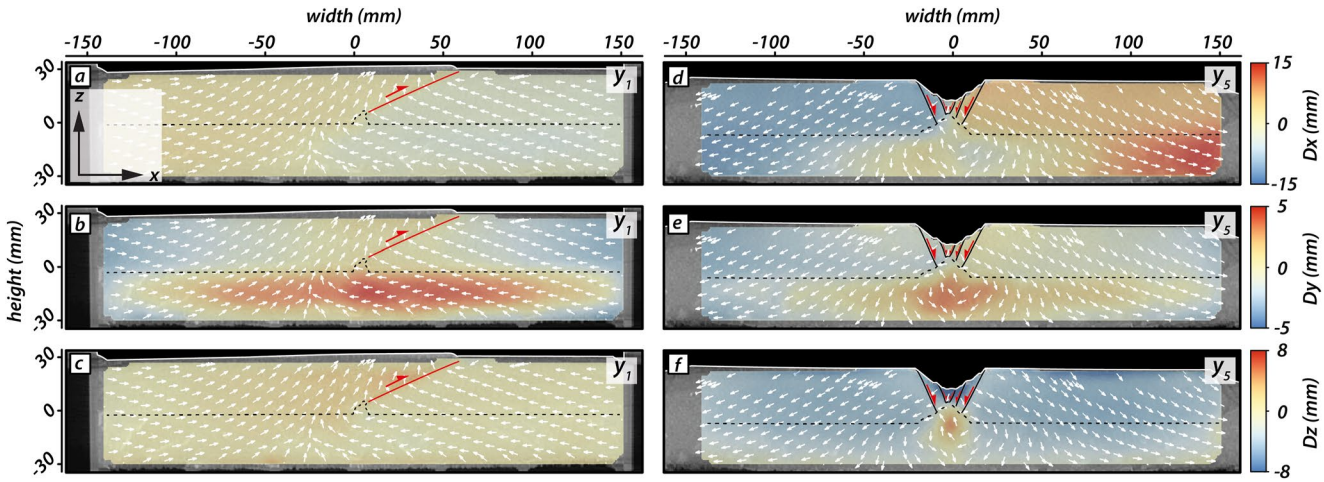


**Figure 10.** Cumulative displacement components for model M1-0*. (a and d) Horizontal displacement component *Dx* at position $y_1$ and $y_5$ in the contractional and extensional domain, respectively. (b and e) Horizontal out of plane displacement component *Dy* at position $y_1$ and $y_5$ in the contractional and extensional domain, respectively. (c and f) Vertical displacement component *Dz* at position $y_1$ and $y_5$ in the contractional and extensional domain, respectively. Black dashed lines indicate the brittle-ductile interface. Red and black lines indicate thrusting and normal faults, respectively. White arrows indicate the total 3D displacement, projected into the plane. Note the different scale bars on the right-hand side of each displacement component. Convention for orientation of $Y_1$ and $Y_5$ is shown in Figure 4.

The magnitudes of the maximum horizontal displacement component *Dx* are smaller than expected based on the maximum divergence velocity (20 mm/hr on each side). This results partly from the fact that the applied maximum divergence velocity is defined along a circular segment. However, this deviation is on the order of 1% and therefore negligible. More importantly, the DVC analysis does not capture the entire model length (see Figure 2b) and is also limited by a fixed data mask width along the *y* axis and can therefore not account for the increasing differences in model width along the *y* axis over time. Therefore, the DVC analysis cannot capture maximum displacements near the mobile sidewalls (i.e., model widths, −150 and 150 mm) which results in smaller maximum values of the horizontal displacement component *Dx*.

In the contractional domain (Figures 10a–10c), *Dx* values range between −5 and 5 mm (Figure 10a). The left part (i.e., from $x = -150$ to 0 mm) moves to the right (indicated by light red colors) while the right part (i.e., from $x = 0$–150 mm) moves to the left (indicated by light blue colors). This results in a sharp displacement gradient in the brittle domain representing a thrust fault (Figure 10a). The horizontal out of plane displacement *Dy* is distinctly different between the brittle and viscous domains. *Dy* values in the viscous domain range between −5 and 5 mm with positive values indicating flow from the contractional to the extensional domain and vice versa (Figure 10b). In the contractional domain, the *Dy* displacement component is characterized by a wide zone (ca. −100 to 100 mm) of enhanced displacement with values ≤5 mm (Figure 10b). In the brittle domain, *Dy* values are mostly negative indicating a cumulative displacement away from the extensional domain toward the contractional part. Only a central area confined by thrust faults shows positive values (Figure 10b). Vertical displacement values *Dz* are small and generally positive in the contractional domain (Figure 10c), where thrusting in the brittle domain leads to a minor uplift of about 5 mm near the model center (from −50 to 50 mm).

Generally, the horizontal displacement components *Dx* and *Dy* are more pronounced in the extensional domain (Figures 10d–10f). The *Dx* component shows diffuse stretching in the viscous layer, whereas deformation in the brittle layer localizes above the viscous seed, resulting in a graben system (Figure 10d). Note that the displacement polarity changes at the brittle-ductile interface which results in pockets of reversed viscous flow below the rift axis (from ca −50 to 50 mm). The change in the horizontal displacement direction at the brittle-ductile interface is coupled with the vertical displacement *Dz* (Figure 10f). In the viscous layer below the rift zone, the viscous seed material rises, while the surrounding viscous and brittle material subsides due to gravitational unloading in the rift center. The combination of horizontal *Dx*, and vertical *Dz* displacement causes a convection-like cell indicated by the displacement vectors. The horizontal displacement component *Dy* (Figure 10e) has maximum values in the viscous layer below the rift. In contrast to the contractional domain, the zone of pronounced displacement is restricted to the model center.

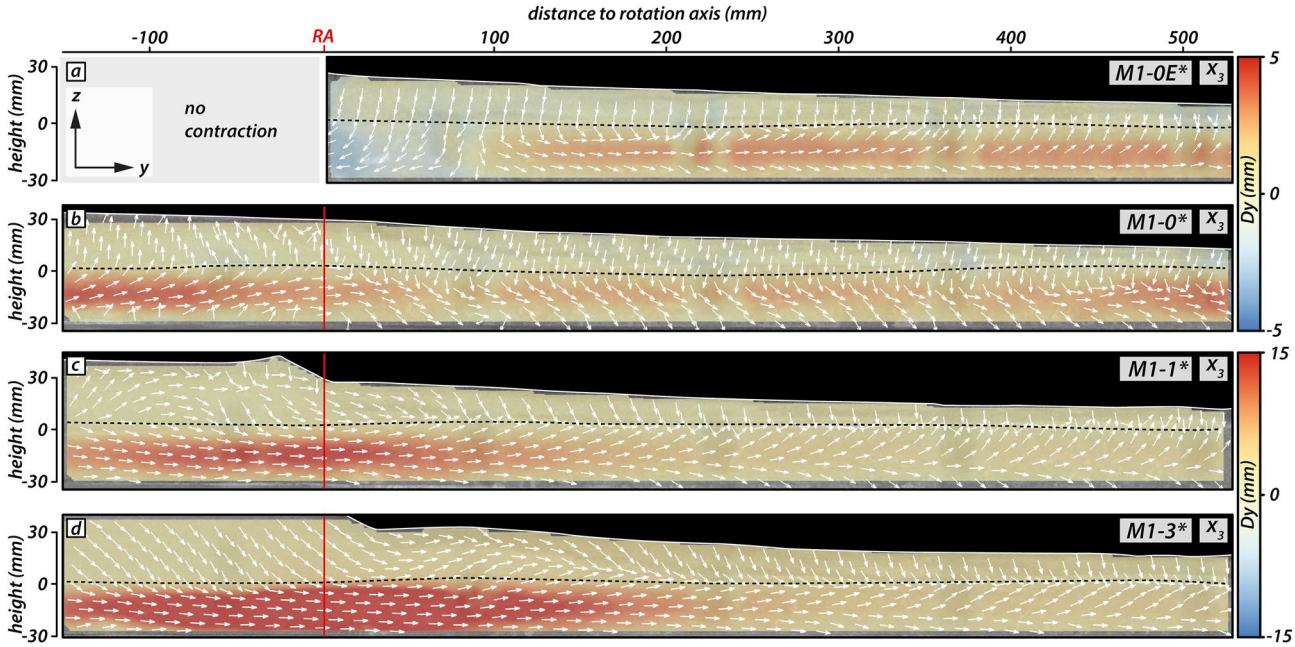


**Figure 11.** Central slice $x_3$ of the horizontal displacement component *Dy* for CT scanned models with a brittle ductile thickness ratio $T_{BD} = 1$ at final stage. (a) Model M1-0E* without contractional domain. (b) Model M1-0*. (c) Model M1-1*. (d) Model M1-3* (additional gravitational load cut off by XRCT scan). With an increasing additional gravitational load, the horizontal displacement component *Dy* increases in the viscous domain and subsequently localizes with maximum displacement values below the topographic step. Dashed line indicates the brittle-ductile interface. White arrows indicate the total 3D displacement, projected into the plane. RA and red vertical line refer to the rotation axis. Note the different scale bars on the right-hand side. For convention of the orientation of the $X_3$ section see Figure 4.

### 3.3.2. Rift-Axis Parallel Horizontal Displacement *Dy* in the $x_3$ Longitudinal Transect

Longitudinal transects of all XRCT scanned models show that the rift-axis parallel horizontal displacement (*Dy*) is focused in the viscous domain (Figure 11). $D_y$ displacement values range between −5 and 5 mm for models M1-0E* (Figure 11a) and M1-0* (Figure 11b), and between −15 to 15 and −30 to 30 mm for models M1-1* (Figure 11c) and M1-3* (Figure 11d), respectively.

For model M1-0E*, maximum values of *Dy* occur in the viscous layer at ∼100 mm from the rotation axis and continue evenly to the extensional domain at the far end at ∼550 mm (Figure 11a). Near the rotation axis (0–100 mm), rift-axis parallel displacement values are negative. Similarly, rift-axis parallel displacement in model M1-0* (Figure 11b) indicates a continuous channel flow with *Dy* values around 3 mm in the center of the viscous layer. However, two distinct zones of maximum values with 5 mm displacement occur in the contractional domain (at −100 mm distance to the rotation axis) and at the far end of the extensional domain (500 mm). In experiments with an additional gravitational load, a continuous channel of rift-axis parallel displacement in the viscous domain is subsequently localized below the topographic step (Figures 11c and 11d). In Model M1-1*, maximum displacement values of 15 mm are located below the topographic step at the rotation axis and gradually decrease to 0 at ∼200 mm distance from the rotation axis (Figure 11c). This is also valid for model M1-3* (Figure 11d). However, in this experiment maximum values of rift-axis parallel displacement double and reach up to 30 mm.

### 3.3.3. Vertical Displacement *Dz* in the $x_3$ Longitudinal Transect

The increased rift-axis parallel displacement in models with an additional gravitational load also affects the vertical displacement component *Dz* (Figures 12c and 12d). In the brittle layer, negative values as large as −8 mm reflect subsidence within the rift. For models without an additional gravitational load (M1-0E*, M1-0*; Figures 12a and 12b), subsidence of the brittle layer occurs across the entire extensional domain and reaches maximum values near the far end at ∼500 mm from the rotation axis. In the viscous layer, maximum values of $Dz = 8$ mm occur near the far end at ∼500 mm and indicate upward flow simultaneously with the thinning of the brittle layer (Figures 12a and 12b; see also Figure 10f). In model M1-0* (Figure 12b), subsidence in the brittle layer decreases toward the rotation axis and changes to uplift in the contractional domain. With an additional

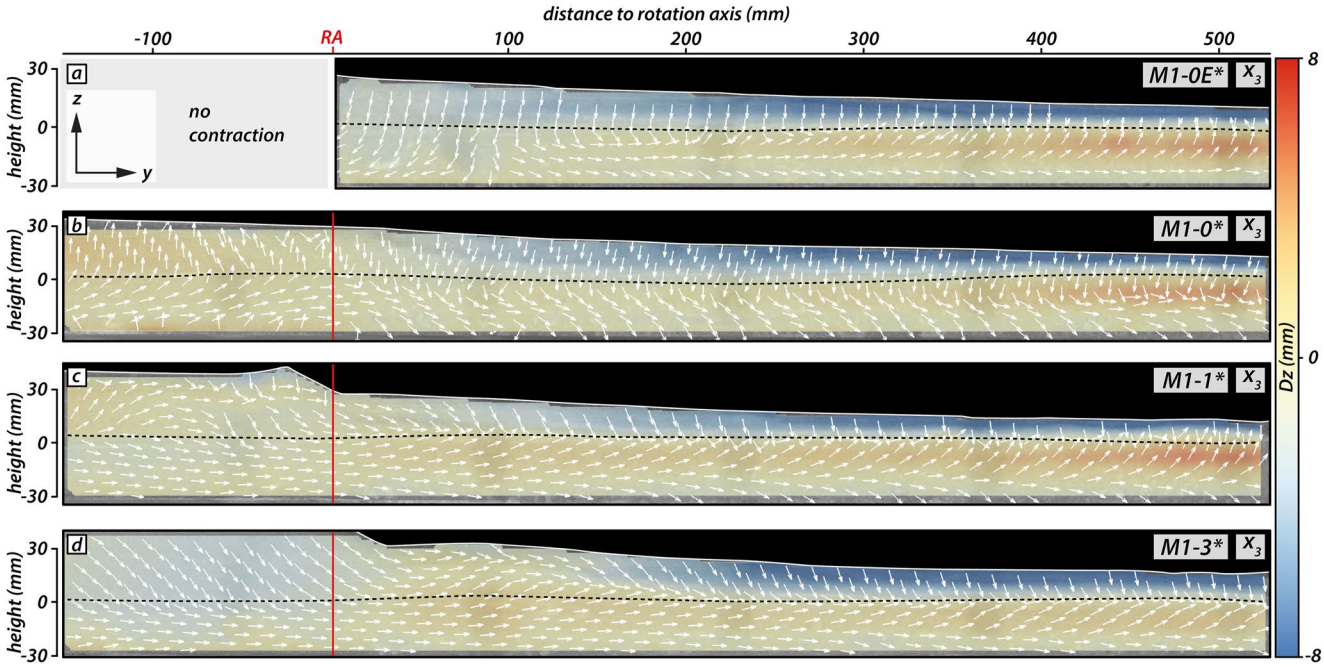


**Figure 12.** Central longitudinal slice $x_3$ of the vertical displacement component $Dz$ for CT scanned models with a brittle-ductile thickness ratio $T_{BD} = 1$ at final stage. (a) Model M1-0E* without contractional domain. (b) Model M1-0*. (c) Model M1-1*. (d) Model M1-3* (additional gravitational load cut off by XRCT scan). With an increasing additional gravitational load, uplift decreases in the contractional brittle domain. Subsidence patterns in the extensional brittle domain coincide with upward flow of the viscous material in the extensional domain. Dashed lines indicate the brittle-ductile interface. White arrows indicate the total 3D displacement, projected into the plane. RA and red vertical lines refer to the rotation axis. For convention of the orientation of the $X_3$ section see Figure 4.

gravitational load of 1 cm (M1-1*; Figure 12c), maximum uplift values in the contractional brittle domain are smaller (compared to models M1-0E* and M1-0*) and eventually are negative in model M1-3*, where subsidence occurs (Figure 12d). While the viscous layer in model M1-1* still shows upward flow near the extensional far end, maximum $Dz$ values are ~0 mm in model M1-3*, where upward flow of the viscous layer is suppressed. However, model M1-3* shows increased vertical displacement in the viscous layer close to the topographic step at ~50 mm from the rotation axis, which also affects vertical motions of the brittle layer (Figure 12d; see also Figure 9h).

## 4. Discussion

In this study, we used DVC in combination with 3D DIC to depict and understand the coupling of near-surface rift development and deep-seated crustal flow in a rotational rift setting. To simulate different initial crustal configurations, we used a series of brittle-ductile thickness ratios $T_{BD}$, where increasing values indicate increasing crustal strengths. Our results show that DVC applied to XRCT images provides a unique opportunity to gain insights on the time-dependent internal deformation of analog models. This method allows for a fully quantitative description of both the surface deformation and the deformation of internal layers representing lower parts of the crust.

A previous study by Zwaan, Schreurs, and Adam (2018) reports DVC analyses performed on crustal scale analog rift models undergoing orthogonal extension. They showed that the interaction between two segmented rift branches caused substantial horizontal displacements in the viscous layer (lower crust analog), parallel to the direction of rift propagation. This shows that slight deviations (i.e., an offset between two parallel rift branches) from a cylindrical setup can result in considerable out of plane displacements. In the case of a rotational model setup, rift-axis parallel displacement components are even more pronounced. Zwaan et al. (2020) used the same experimental apparatus as this study and gave preliminary insights on rift-axis parallel displacement in a rotational system. Although they applied 2D DIC on a single longitudinal XRCT transect (Figure 10b in Zwaan et al., 2020), rift-axis parallel displacement patterns in our model M1-0* agree well with their findings. We also observe a similar enhanced horizontal $Dy$ displacement in our model M1-0E* (see Figures 11a , 11b and 14b)

from which we conclude that the contracting boundary sidewalls in our experimental apparatus do not influence displacement patterns in the extensional domain. Rift-axis parallel flow has also been documented in lithospheric scale numerical models (e.g., Le Pourhiet et al., 2018; Van Wijk & Blackman, 2005), highlighting the importance of out of plane displacement components even in models with reasonably cylindrical boundary conditions.

### 4.1. The Influence of Rift-Axis Parallel Horizontal Flow on Rift Propagation

The presence of a horizontal pressure gradient (resulting from a topographic load at the contractional end of the model domain) influences the evolution of the rift structure. Figures 7 and 8 illustrate the delay in rift evolution in terms of rift tip propagation, the timing of the abandonment of rift boundary faults and successive initiation of faulting activity along intra-rift faults (inward migration). To understand the cause of such delayed evolution, we consider deformation in the viscous layer. Figures 11 and 12 show the rift-axis parallel horizontal displacement $Dy$, and the vertical displacement component $Dz$, respectively. The subsiding brittle layer in the extensional domain is coupled with an upward flow of the viscous material underneath the rift axis (Figure 12). For increasing additional gravitational loads, the $Dz$ upward flow component appears to be perturbed and overprinted by a strong rift-axis parallel horizontal flow component $Dy$ (Figure 12d). T. C. Schmid, Schreurs, and Adam (2022) propose that intra-rift faults initiate early as antithetic faults but remain largely passive while slip is accommodated along the rift boundary faults. It is only after they reach the brittle-ductile interface, where shear stresses are high (Corti et al., 2010), that intra-rift faults accommodate considerable displacement and concomitant fault activity along the rift boundary faults decreases. Hence, the upward flow of the viscous material increases and facilitates further activation of intra-rift faults. Zwaan, Schreurs, and Adam (2018) showed the inhibiting effect of syn-rift sedimentation on the ascent of viscous material below the rift structure. Although we do not consider the effect of sedimentation, the presence of a large additional gravitational load induces a dominant rift-axis parallel horizontal displacement component $Dy$, which is strong enough to overprint or inhibit vertical upward flow of the viscous material. This effect delays rift evolution, as expressed by retardation of rift tip propagation, inward fault migration, and activation of intra-rift faults.

### 4.2. Effect of Deep-Seated Deformation on Surface Topography and Rift Evolution

Surface analyses show that increasing the brittle-ductile thickness ratio $T_{BD}$ has no recordable influence on rift evolution in models with an initial flat topography (Figures 7 and 9). However, in models with an additional gravitational load, we observe enhanced vertical motions close to the rotation axis (Figure 9) as well as horizontal motions. Such horizontal motions at the surface are especially prominent in models with an intermediate or low brittle-ductile thickness ratio $T_{BD}$ (Figures 9g–9j). For XRCT scanned models with $T_{BD} = 1$, this observation is consistent with the internal displacement fields (Figures 10–12) and is likely governed by increased flow in the viscous layer of the model and, the additional gravitational load. This becomes evident when rewriting Equation 1 in terms of the volumetric flow rate

$$Q = -\frac{h^3}{12\mu}\frac{dp}{dx}. \tag{6}$$

where $\mu$ is the viscosity that is required to maintain horizontal flow in a channel with thickness $h$, driven by a lateral pressure gradient $dp/dx$, along the horizontal length of the channel to minimize lateral variations in thickness (e.g., Kruse et al., 1991; Turcotte & Schubert, 1982). The proportionality $\mu \sim h^3$ in Equation 6 requires lower viscosities for smaller channel thicknesses to maintain a constant volumetric flow rate $Q$, when other parameters are kept constant. Since we use models with constant viscosity, a larger channel thickness (i.e., lower $T_{BD}$) results in enhanced horizontal flow and hence, enables more surface deformation. We must emphasize therefore that it is the absolute thickness of the viscous layer (in addition to viscosity and pressure gradient), rather than the brittle-ductile thickness ratio, that is the principal determinant for the magnitude of lower crustal flow.

This enhanced lower crustal channel flow is ultimately expressed by increased vertical motions in models with an intermediate to low $T_{BD}$ (Figures 9 and 13). Regardless of the brittle-ductile thickness ratio, local contraction results in a zone of uplift in models with flat initial topography (Figures 9a–9e and 13a). However, in models with an additional gravitational load (Figures 9f–9j and 13–13e), the intensity of vertical motion at the surface increases in experiments with thick viscous layers (i.e., $T_{BD} = 0.5$). While models with thin viscous layers (i.e.,

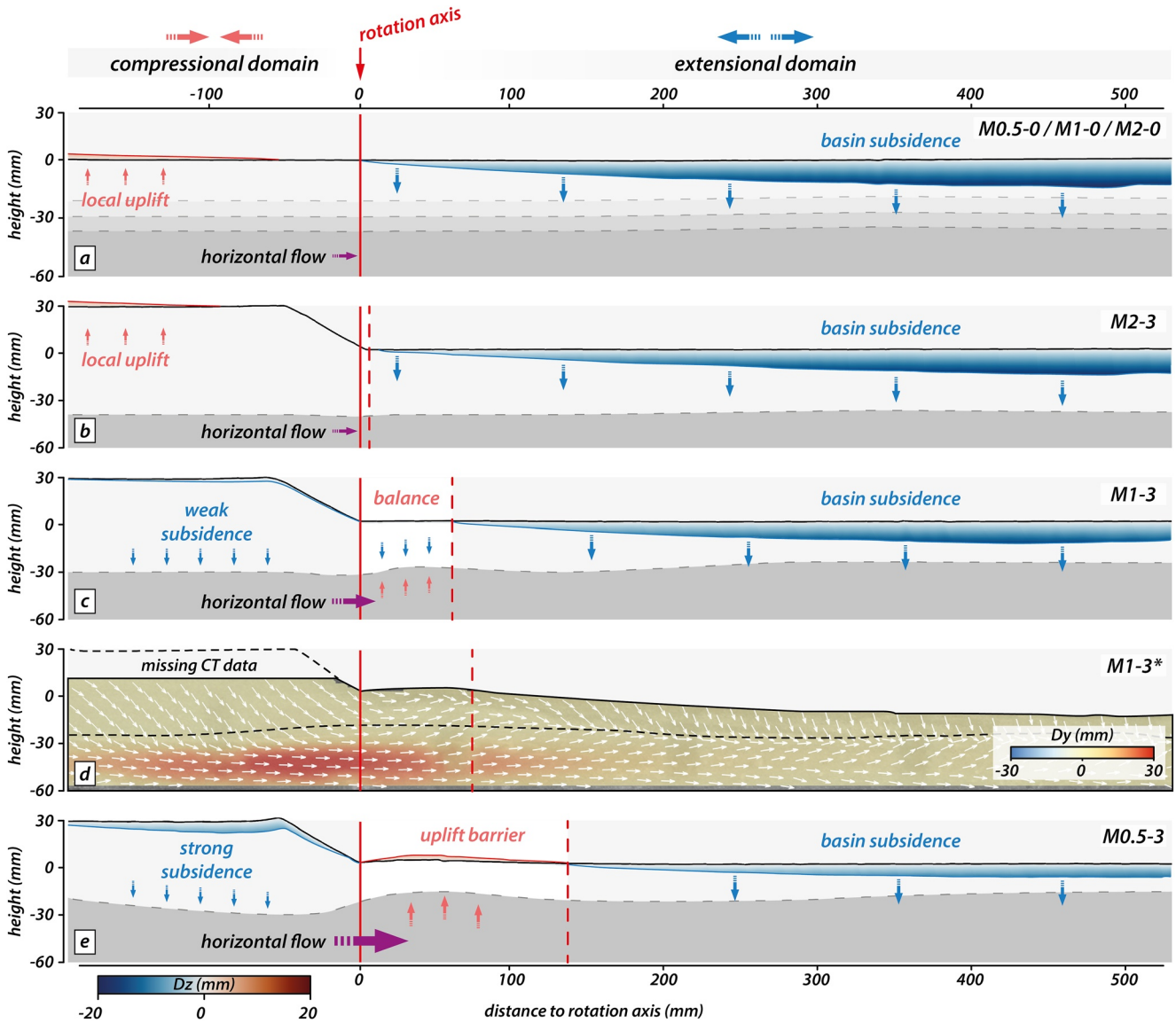


**Figure 13.** Longitudinal transects through the rifted area showing the effect of the brittle ductile ratio $T_{BD}$ on the final topography. (a) Representative model with $T_{BD} = 1$ and an initial flat topography. Various black, dashed lines indicate the brittle ductile interface for different brittle ductile ratios. (b) Model with $T_{BD} = 2$ and gravitational load of 3 cm. (c) Model with $T_{BD} = 1$ and gravitational load of 3 cm. (d) Digital Volume Correlation transect from model M1-3* of the horizontal displacement component *Dy*at the same position as in panel (c). (e) Model with $T_{BD} = 0.5$ and tectonic load of 3 cm. Colors at the surface indicate vertical motions and are obtained from 3D stereo Digital Image Correlation. Vertical red solid lines indicate the position of the rotation axis, which coincides with the separation of uplift and subsidence in models with a flat topography. With decreasing $T_{BD}$, the horizontal displacement component *Dy*increases, causing a horizontal flow component in the viscous layer which accommodates vertical motions in the brittle layer. Vertical red dashed lines indicate the protruding zone of uplift in the extensional domain with increasing channel thickness (i.e., decreasing $T_{BD}$). Topography of the viscous layer is supported by XRCT data and digital elevation models from the top of the viscous layer after the model runs.

$T_{BD} = 2$) still yield net uplift in the contractional domain (Figures 9f and 13b), models with viscous layers of intermediate thickness (i.e., $T_{BD} = 1$) show a net subsidence (Figures 9g–9j and 13c–13e). In these models the channel thickness is sufficient to maintain a rift-parallel, horizontal channel flow component which transports material away from the contractional domain, counteracting the tectonic uplift caused by contraction (Figures 9g–9j and 13c–13e). This results in a net subsidence in the contractional domain and, where the horizontal flow component decreases, the excess material in the lower crust enables synchronous uplift during extension while rifting occurs. In the extreme case (i.e., thick viscous layer; $T_{BD} = 0.5$), uplift raises the propagating rift tip above its original elevation, resulting in net uplift of the rift system when crossing the uplift barrier (Figures 9j and 13e).

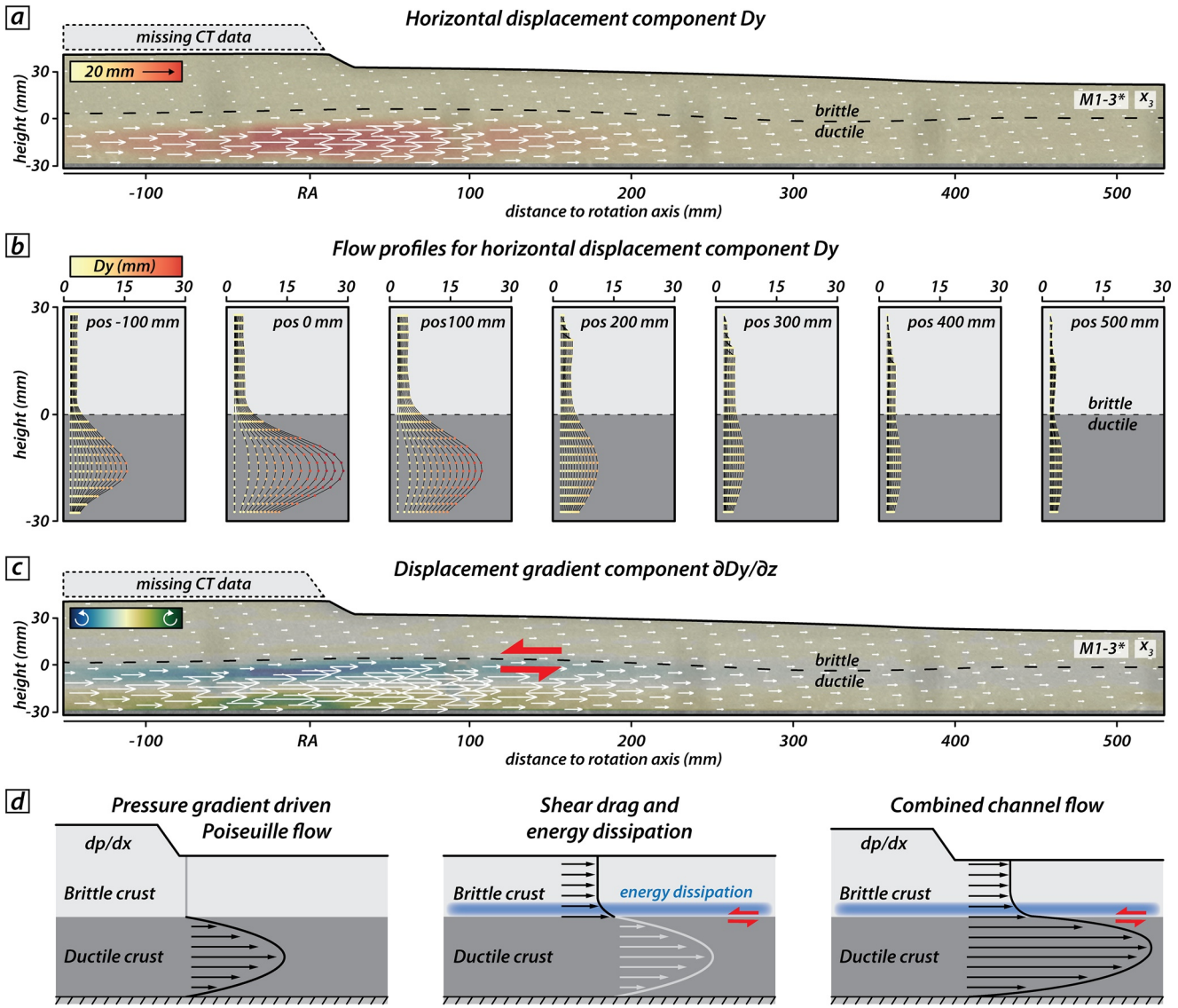


**Figure 14.** Rift-axis parallel horizontal displacement *Dy* in the $x_3$ longitudinal transect of model M1-3* and conceptual flow model. (a) Longitudinal CT slice through the central part and displacement data obtained from Digital Volume Correlation analysis. Contours and white arrows both indicate the horizontal displacement component *Dy*. The black dashed line marks the brittle-ductile interface. RA indicates the rotation axis. (b) Vertical profiles along the central longitudinal $X_3$ transect at indicated positions. Black lines show the horizontal displacement component, *Dy*, with depth at 20 min intervals with marker colors referring to the magnitude of *Dy*. (c) Longitudinal CT slice through the central part and horizontal displacement gradient component $\partial Dy/\partial z$, which indicates shearing along the brittle-ductile interface. Counter-clockwise rotation causes a top-to-left shear sense (red half arrows) at the brittle-ductile interface (black dashed line). White arrows indicate the horizontal displacement component *Dy*. RA indicates the position of the rotation axis along the *x* axis. (d) Conceptual flow model for rift-axis parallel flow, based on data shown in panels (a–c). The pressure-gradient (due to an additional gravitational load and/or the increased thinning away from the rotation axis) induces a Poiseuille from the contractional domain toward the extensional domain resulting in a parabolic flow profile in the viscous layer (left panel). Flow in the viscous layer drags the brittle upper layer and moves it into the direction of viscous flow. Shearing along the brittle-ductile interface results in a thin boundary zone in the brittle layer, where energy dissipation occurs (middle panel). Energy dissipation at the brittle-ductile interface results in reduced *Dy* values in the brittle layer that moves as a rigid block (right panel).

### 4.3. Conceptual Model for Rift-Axis Parallel Flow

The insights from the experiments on how lower crustal flow interacts with upper crustal deformation allow us to develop a flow model for our rotational extension experiments. In our experiments, rift-axis parallel horizontal displacement velocities calculated from DVC analyses are systematically higher compared to theoretical values obtained from Equation 1. At the central longitudinal transect ($X_3$) of model M1-3* (i.e., 1 cm additional gravitational load) for example, maximum *Dy* values at the final stage occur close to the topographic step and are

~30 mm (Figure 14a). However, theoretical values for Poiseuille flow (Equation 1) yield a maximum *Uy* velocity of ~3.75 mm $hr^{-1}$ resulting in maximum *Dy* values of ~15 mm. For model M1-1* (i.e., 1 cm additional gravitational load) measured maximum *Dy* values are ~15 mm, whereas Equation 1 yields a maximum *Uy* velocity of ~1.25 mm $hr^{-1}$ that translates to a maximum *Dy* value of ~5 mm at the final stage. For models without an additional gravitational load, measured maximum *Dy* values are ~5 mm and Equation 1 predicts 0 mm. Interestingly, the differences between measured and theoretical values are systematically larger with increasing additional gravitational loads. This discrepancy can be attributed to two causes: First, the rotational opening of the experimental apparatus provokes rift-axis parallel flow away from the rotation axis even without an additional gravitational load (Figures 10, 11 and 14). Second, the strong rift-axis parallel displacement component measured at the model surface (gray arrows Figures 9g–9j) indicates that the contact between the brittle and viscous layers is not a fixed boundary (with respect to the viscous layer) and therefore allows higher flow velocities in the viscous domain than expected in the case of pure Poiseuille flow.

Figure 14b shows *Dy* profiles through the brittle and viscous layers at distinct positions along the rift axis. The effect of the pressure gradient (i.e., parabolic shape of the displacement profile) is evident in the viscous layer near the topographic step and decreases farther away from the rotation axis in the extensional domain. The brittle layer shows uniform *Dy* values through the entire layer thickness indicating that the brittle layer moves as a rigid block. It is only in a thin layer at the brittle-ductile interface, where a displacement gradient in the granular material occurs. This transition is likely due to energy dissipation and is expressed by enhanced shear strain, which reduces displacement values in the brittle layer compared to the viscous layer (Figure 14c). The displacement gradient *dDy*/*dz* reveals anticlockwise rotation at the brittle-ductile transition indicating a top-to-left shear sense (red arrows; Figure 14c).

The general equation for the velocity, $u$, in a planar Couette flow of a linear viscous fluid in a channel with thickness $h$, viscosity $\mu$, and an applied horizontal pressure gradient $dp/dx$ is:

$$u(z) = \frac{1}{2\mu}\frac{dp}{dx}\left(z^2 - hz\right) + \frac{u_0 z}{h}. \tag{7}$$

where $u_0$ is the relative velocity between channel and bounding plates (Turcotte & Schubert, 1982). In the case of Poiseuille flow, the bounding plates are fixed and $u_0 = 0$, such that the lateral pressure gradient produces a parabolic velocity profile with maximum values in the center of the channel (Figure 14d, left panel). We have shown above that rift-axis parallel viscous flow in our experiments is not confined by fixed bounding plates (i.e., the brittle layer moves as well), which ostensibly agrees with a Couette flow component in addition to pressure-gradient driven Poiseuille flow. However, there is a fundamental difference between the flow described in Equation 7 and the rift-axis parallel flow observed in our experiments. For Couette flow, the upper boundary moves and drives flow in the viscous layer below. In the case of our experiments, however, it is the viscous layer that exerts a drag force on the brittle layer, resulting in energy dissipation due to shearing at the brittle-ductile interface (Figure 14d, middle panel). It is this shearing, which ultimately causes a difference in the *Dy* values in the viscous and brittle layer (Figure 14d, right panel).

### 4.4. Coupling Between Brittle and Viscous Layers During Rift-Axis Parallel Displacement

The horizontal displacement field at the surface of models with an additional gravitational load is systematically different to those of all models with an initial flat topography (Figure 9). Such modified horizontal displacements indicate a rift-axis parallel overprint, similar to those observed in longitudinal DVC transects (Figures 11 and 14). However, as discussed above, the rift-axis-parallel displacement component at the model surface is reduced compared to the displacement component in the viscous part of the model suggesting a degree of brittle-viscous decoupling between the two model layers (sensu Zwaan et al., 2019).

To further investigate the mechanical coupling of brittle and ductile deformation during rifting, we use the quantitative results for models with $T_{BD} = 1$ and compare the evolution of the rift-axis parallel mean values in the brittle (Figure 15a) and viscous domain (Figure 15b). We restrict the investigation to a 10 cm wide central area (i.e., close to the $X_3$ longitudinal transect; Figures 11 and 14) in the extensional domain to exclude displacement effects due to rotational opening.

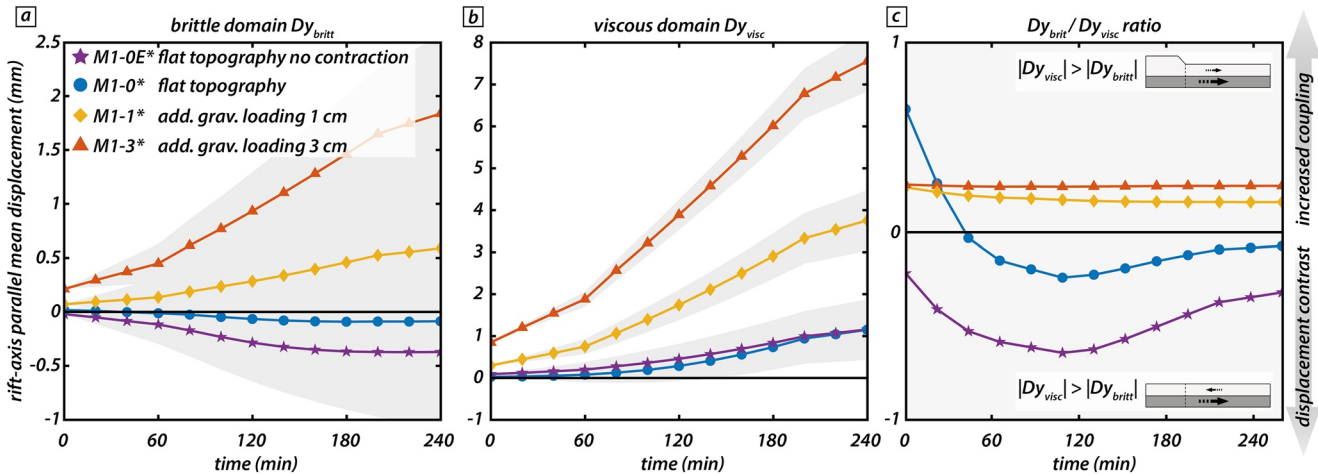


**Figure 15.** Evolution of mean values of the rift-axis parallel displacement *Dy* obtained from Digital Volume Correlation analyses on XRCT scanned models with identical $T_{BD} = 1$ (i.e., a 3 cm thick viscous lower crust). (a) Evolution of rift-axis parallel mean displacement in the brittle ($Dy_{britt}$) and (b) viscous domain ($Dy_{visc}$), respectively. Gray bands indicate uncertainties for corresponding models. For mean displacement calculations, only a 10 cm wide central channel in the extensional part of the model setup is considered. Positive and negative values indicate rift-axis parallel displacement away from and toward the rotation axis, respectively. (c) Ratio between rift-axis parallel displacements in the brittle and viscous domain as a proxy for brittle-viscous coupling between both model layers. Values above the 0 indicate identical displacement directions, whereas values below indicate opposing displacements in the brittle and viscous model layer.

The rift-axis parallel displacement in the brittle domain (Figure 15a) shows positive and negative trends for models with (i.e., M1-1* and M1-3*) and without (i.e., M1-0* and M1-0E*) an additional gravitational load, respectively. However, for model M1-0*, this negative trend is negligible, within the error. Note that positive and negative values indicate mean displacements toward and away from the location of maximum opening, respectively. In the viscous domain, mean values all show positive trends indicating rift-axis parallel flow toward the location of maximum opening. Plotting the evolution of the ratio between mean values from the brittle and viscous domain (Figure 15c) reveals the degree of brittle-viscous coupling between the two model layers with respect to rift-axis parallel displacements. If the mean *Dy* values of the brittle and viscous layer in one experiment are totally coupled, this ratio should be 1. Any ratio below 1 indicates an increasing contrast between the rift-axis parallel displacement in the brittle and viscous layer. Positive ratios <1 indicate displacement directions in the viscous domain are larger than those in the brittle domain. Any ratio <0 indicates opposing displacement directions in the brittle and viscous layers. Note that absolute values of mean displacements in the viscous domain are always larger than in the brittle domain and hence, all ratios plot between −1 and 1.

In the case of an additional gravitational load (i.e., M1-1* and M1-3*), both displacement directions are away from the rotation axis toward the extensional domain. The proportional increase in both brittle and viscous *Dy* values is expressed by a constant ratio of ∼0.2. This suggests that for both experiments, rift-axis parallel displacements in the brittle domain are reduced by a factor of 5 in contrast to the viscous flow below the rift. Interestingly, this ratio only increases by a small amount for a larger gravitational load. The increased flow in the viscous domain seemingly affects the rift-axis parallel displacement in the brittle domain equally, regardless of the gravitational load.

For models without an additional gravitational load, negative ratios indicate opposing displacement directions in the brittle and viscous layers. However, the evolution documents an early phase (up to ca 100 min) with continuously increasing displacement contrasts suggesting a first phase of increased decoupling (Figure 15c). After this early phase, ratios increase for both models as *Dy* mean values in the viscous domain increase faster than *Dy* mean values in the brittle layer decrease (i.e., become more negative). We speculate that in this later phase the intensified viscous flow (away from the rotation axis) is due to the increased differential topography along the rift axis which counteracts the opposing *Dy* displacement in the brittle domain. Eventually, the viscous flow likely diminishes the negative *Dy* mean values in the brittle layer such that it flips the direction and hence, increases the brittle-viscous coupling.

Rift tip propagation governed by growth of the rift boundary faults occurs during the early stages of model runs (within 20%–30% of the model runtime; Figure 7; see also Jackson et al., 2017; Rotevatn et al., 2019; T. C.

Schmid, Schreurs, & Adam, 2022). In our experiments M1-0E* and M1-0* the corresponding rift tip propagation does not deviate substantially from those of other experiments (Figure 7). It therefore appears that the increase in coupling between *Dy* mean values in the brittle and viscous layers (after ca 120 min) occurs too late during the model runs to significantly influence lateral rift propagation. Nevertheless, the evolution of the coupling between *Dy* mean values in the brittle and viscous layers in models M1-0E* and M1-0* highlights that it is not a static but rather dynamic process which may change during progressive rotational extension.

### 4.5. The Role of Rift-Axis Parallel Crustal Flow in Natural Settings

Our XRCT scanned models show a substantial amount of rift-axis parallel displacement in the viscous domain (Figures 10, 11, 14 and 15). Also in the absence of a gravitational load, we observe rift-parallel, central flow channels with maximum *Dy* values up to 5 mm (Figure 11) and mean values of ~1 mm (Figure 15) during 40 mm of rift extension. Based on our scaling, this translates to maximum and mean flow velocities of 2 and 0.4 mm/a in nature, respectively. Such values may seem minor when compared to the orthogonally oriented divergence velocity (i.e., 8.8 mm/a) but are they negligible? Various studies have documented, an out-of-plane flow component in the lower crust and its implications on rift evolution (e.g., Amato et al., 2004; Gautier et al., 2008; Little et al., 2011; MacCready et al., 1997; P. D. Clift, 2015).

Based on gravitational potential and buoyancy considerations, Clift (2015) proposes rift-parallel lower crustal flow from the continental crust toward the oceanic rift propagator in the Woodlark Basin as well as in the South China Sea, similar to observations in our analog models. In addition, Little et al. (2007, 2011, 2013) conclude for the Woodlark basin that, based on structural data from the D'Entrecasteaux Islands, regional, lower crustal flow parallel to the rift-axis must have been largely decoupled from the general NNW-SSE extension direction between the Woodlark microplate and the Australian plate (Little et al., 2011). The exhumed gneiss domes on the D'Entrecasteaux Islands show depth-dependent trends in stretching lineation orientation, indicating rift-axis parallel lower crustal flow toward the Papuan Peninsula in contrast to a dominant rift-axis normal stretching lineation in upper crustal levels (Little et al., 2011). The proposed flow direction (based on shear fabrics) for rift-parallel flow is opposite of what we observe in our rotational models and may be explained by asthenospheric inflow into the thinned crust (Abers et al., 2002; Little et al., 2011; Mondy et al., 2018), which we do not consider in our models. The rotational experiment by Mondy et al. (2018) documents a prominent rift-axis parallel flow component in the asthenosphere following the tip of the propagating rift toward the rotation axis. Simultaneously, vertical upward flow compensates for the thinning crust and impedes rift-axis parallel flow in the lower crust away from the rotation axis (Mondy et al., 2018). Interestingly, in early stages of the experiment presented in Mondy et al. (2018), the rift-axis parallel flow component of the asthenosphere is directed toward the extensional far end. However, the authors do not state its effect on lower crustal flow. In our models, we use a rigid basal setup and therefore cannot account for the effect of the asthenosphere on the general model evolution. In this regard, one could argue that our models represent an early stage of continental rifting, where the role of the asthenospheric flow is negligible.

Despite these two contrasting suggestions from Clift (2015) and Little et al. (2011) for the rift-axis parallel lower crustal flow direction, field data from gneiss domes in core complexes on the D'Entrecasteaux Islands is key for uncovering coeval but orthogonal extension directions at varying crustal levels (i.e., rift-axis parallel lower or mid crustal flow and rift-axis perpendicular stretching in the upper crust). The documentation of two orthogonally oriented stretching lineations in such gneiss domes also led other authors to propose the existence of rift-axis parallel lower crustal flow, orthogonal to the regional extension direction (e.g., Amato et al., 2004; Gautier et al., 2008; MacCready et al., 1997). MacCready et al. (1997) document rift-axis parallel northward flow of the middle crust in the Ruby Mountains, Nevada as a response to a rift-axis parallel extension gradient with increasing upper crustal stretching values toward the north. Similarly, Gautier et al. (2008) document in the Nigde Massif, Turkey, rift-axis parallel, lower crustal flow (perpendicular to the extension direction) and determine a northerly flow because of an extension gradient with increasing values toward the northern end of the basin. In both cases, the driving mechanism of regional flow seems to be an extension gradient in which rift-axis parallel lower crustal flow compensates greater thinning of the upper crust. Both settings have kinematic boundary conditions that cause rift-axis parallel lower crustal flow toward areas with higher extension, identical to what we document in our models. Gautier et al. (2008) describe such rift-axis parallel flow as regional-scale lateral channel flow, in contrast to a more local-scale lateral inward flow toward the rift axis, which compensates

thinning of the upper crust parallel to the extension direction (Block & Royden, 1990). Similarly, we observe rift-perpendicular (Figure 10d) and rift-axis parallel (Figures 10e and 11) horizontal flow components in addition to vertical upward flow (Figures 10f and 12) in our models. Eventually, the combination of all displacement components (as documented in nature as well as in our models) give rise to complex 3D flow patterns which can transport a considerable amount of material in or out of a 2D plane. This effect clearly must be considered when estimating crustal extension from 2D rift-perpendicular cross sections (P. D. Clift, 2015).

## 5. Conclusion

We performed a series of brittle-viscous analog models of rotational rifts with an extension gradient in which gravitational loading causes a pressure-gradient driven rift-axis parallel horizontal flow in the lower viscous layer, which is synchronously with rift development in the upper brittle layer. From these experiments we gain insights on the interplay of brittle and ductile deformation in natural rifts that have formed under the influence of along strike extension gradients. The analysis of ductile (deep-seated) and brittle (near-surface) deformation by means of DVC and 3D stereo DIC, respectively provides a quantitative and comprehensive picture of progressive deformation in the experiments. This approach allowed us to detect mechanisms in the viscous model layer that influence the near-surface brittle deformation and eventually cause delayed rift propagation. This results in important implications for the role of crustal flow in natural rift settings, summarized below.

- When compared to models with an initial flat topography, gravitational loading influences the timing of inward migration of faults and retards activation of intra-rift faults. Hence, models with an additional gravitational load show less advanced rift maturity after an identical run time when compared to flat topography models. However, this does not affect lateral rift propagation, regardless of the brittle-ductile thickness ratio $T_{BD}$.
- Models with initial flat topography develop rift structures with subsiding basins in the extensional domain and uplifted areas confined by thrusts in the contractional domain. These patterns are identical for all brittle-ductile thickness ratios. Additional gravitational loading, however, enhances vertical displacements and changes patterns of subsidence and uplift. Subsidence due to gravitational loading drives horizontal flow in the viscous model layer, which results in uplifted areas in the extensional model domain.
- For thicker lower viscous layers, flow channels are larger and hence provide more space for enhanced horizontal ductile channel flow. If an additional gravitational load is applied, this creates more pronounced uplift in the extensional domain.
- Enhanced rift-axis parallel flow in the viscous model layer overprints vertical upward flow near the rift axis. Upward flow originally helps to activate intra-rift faults and drives inward fault migration. Hence, viscous rift-axis parallel delays inward migration of activity along faults and enables boundary faults to be active for a longer time. This results in a comparatively less mature rift stage at a given time.
- Rift-axis parallel flow in the viscous model domain is driven by a pressure gradient due to differential topography (Poiseuille flow). Viscous flow drags the brittle upper layer as a rigid block. Shearing occurs along the brittle-ductile interface where energy dissipation results in reduced *Dy* displacement values compared to *Dy* displacement values in the viscous layer.
- DVC depicts enhanced horizontal rift-axis parallel flow patterns in the viscous domain for models with additional gravitational loads. Correlation between growing mean values of rift-axis-parallel displacement components in the viscous and brittle layer, shows different degrees of coupling between these two domains. For models with an additional gravitational load, stable mechanical coupling (of some degree) between the brittle and ductile layer is expressed by identical displacement directions toward the extensional domain. In models without additional gravitational loads, mechanical coupling is transient and changes during the model run, showing that this is a dynamic process, rather than a static one.
- Rift-axis parallel ductile flow, documented in rift settings with an extension gradient, results in material transport out of the rift transect. When scaled to nature, displacements from our models confirm substantial outflow of lower crustal material parallel to the rift axis. This mechanism may explain discrepancies between subsidence estimates based on upper crustal extension and subsidence in profiles and emphasizes the three dimensionality of rifting.

## Data Availability Statement

Rheological measurements of the brittle and viscous materials used in this study are available in the form of open access data publications via GFZ Data Services (T. Schmid et al., 2020a, 2020b; Zwaan, Schreurs, Ritter, et al., 2018, respectively). An additional open access data publication on the GFZ Data Service (T. C. Schmid, Rudolf, et al., 2022) provides additional images and movies of our models. Links to these data sets are provided in the reference list.

**Acknowledgments**
The authors thank Sandy Cruden and Anouk Beniest for thorough reviews of the original manuscript. The DIC analyses are part of an EPOS TCS MSL Trans-National Access project and were performed at the HELTEC lab at the GFZ Potsdam. The authors thank Matthias Rosenau and Michael Rudolf for providing access to and assistance in operating DaVis 8.4 and thank Nicole Schwendener for operating and assisting us with the XRCT machine. The authors are grateful for helpful discussions with Frank Zwaan and Peter Clift. This project is supported by the Swiss National Science Foundation (Grant No. 200021_178731). The authors thank the Berne University Science Foundation for financial support of the rotational extension machine (Grant No. 2015-19). Open access funding provided by Universitat Bern.

## References

Abers, G. A., Ferris, A., Craig, M., Davies, H., Lerner-Lam, A. L., Mutter, J. C., & Taylor, B. (2002). Mantle compensation of active metamorphic core complexes at Woodlark Rift in Papua New Guinea. *Nature*, *418*(6900), 862–865. https://doi.org/10.1038/nature00990

Adam, J., Klinkmüller, M., Schreurs, G., & Wieneke, B. (2013). Quantitative 3D strain analysis in analogue experiments simulating tectonic deformation: Integration of X-ray computed tomography and digital volume correlation techniques. *Journal of Structural Geology*, *55*, 127–149. https://doi.org/10.1016/j.jsg.2013.07.011

Adam, J., Urai, J., Wieneke, B., Oncken, O., Pfeiffer, K., Kukowski, N., et al. (2005). Shear localisation and strain distribution during tectonic faulting—New insights from granular-flow experiments and high-resolution optical image correlation techniques. *Journal of Structural Geology*, *27*(2), 283–301. https://doi.org/10.1016/j.jsg.2004.08.008

Amato, J. M., Miller, E. L., & Whitney, D. (2004). Geologic map and summary of the evolution of the Kigluaik Mountains gneiss dome, Seward Peninsula, Alaska. *Special Papers – Geological Society of America*, 295–306. https://doi.org/10.1130/0-8137-2380-9.295

Benes, V., Scott, S. D., & Binns, R. A. (1994). Tectonics of rift propagation into a continental margin: Western Woodlark Basin, Papua New Guinea. *Journal of Geophysical Research*, *99*(B3), 4439–4455. https://doi.org/10.1029/93JB02878

Block, L., & Royden, L. H. (1990). Core complex geometries and regional scale flow in the lower crust. *Tectonics*, *9*(4), 557–567. https://doi.org/10.1029/TC009i004p00557

Buck, W. R. (1991). Modes of continental lithospheric extension. *Journal of Geophysical Research*, *96*(B12), 20161–20178. https://doi.org/10.1029/91JB01485

Byerlee, J. (1978). *Friction of rocks, rock friction and earthquake prediction* (pp. 615–626). Springer. https://doi.org/10.1007/978-3-0348-7182-2_4

Clark, M. K., & Royden, L. H. (2000). Topographic ooze: Building the eastern margin of Tibet by lower crustal flow. *Geology*, *28*(8), 703–706. https://doi.org/10.1130/0091-7613(2000)28<703:TOBTEM>2.0.CO;2

Clift, P., Lin, J., & Barckhausen, U. (2002). Evidence of low flexural rigidity and low viscosity lower continental crust during continental break-up in the South China Sea. *Marine and Petroleum Geology*, *19*(8), 951–970. https://doi.org/10.1016/S0264-8172(02)00108-3

Clift, P. D. (2015). Coupled onshore erosion and offshore sediment loading as causes of lower crust flow on the margins of South China Sea. *Geoscience Letters*, *2*, 1–11. https://doi.org/10.1186/s40562-015-0029-9

Clift, P. D., Brune, S., & Quinteros, J. (2015). Climate changes control offshore crustal structure at South China Sea continental margin. *Earth and Planetary Science Letters*, *420*, 66–72. https://doi.org/10.1016/j.epsl.2015.03.032

Corti, G., Ranalli, G., Mulugeta, G., Agostini, A., Sani, F., & Zugu, A. (2010). Control of the rheological structure of the lithosphere on the inward migration of tectonic activity during continental rifting. *Tectonophysics*, *490*(3–4), 165–172. https://doi.org/10.1016/j.tecto.2010.05.004

Gautier, P., Bozkurt, E., Bosse, V., Hallot, E., & Dirik, K. (2008). Coeval extensional shearing and lateral underflow during Late Cretaceous core complex development in the Niğde Massif, Central Anatolia, Turkey. *Tectonics*, *27*(1), TC1003. https://doi.org/10.1029/2006TC002089

GEBCO Compilation Group. (2021). *The GEBCO_2021_Grid – A Continuous Terrain Model of the Global Oceans and Land*. National Oceanography Centre, NERC Atlanta. Retrieved from https://www.gebco.net

Hubbert, M. K. (1937). Theory of scale models as applied to the study of geologic structures. *The Geological Society of America Bulletin*, *48*(10), 1459–1520. https://doi.org/10.1130/GSAB-48-1459

Jackson, C. A.-L., Bell, R. E., Rotevatn, A., & Tvedt, A. B. (2017). Techniques to determine the kinematics of synsedimentary normal faults and implications for fault growth models. *Geological Society, London, Special Publications*, *439*(1), 187–217. https://doi.org/10.1144/SP439.22

Klinkmüller, M. (2011). *Properties of analogue materials, experimental reproducibility and 2D/3D deformation quantification techniques in analogue modelling of crustal-scale processes* (Ph.D. thesis). University of Bern.

Kruse, S., McNutt, M., Phipps-Morgan, J., Royden, L., & Wernicke, B. (1991). Lithospheric extension near Lake Mead, Nevada: A model for ductile flow in the lower crust. *Journal of Geophysical Research*, *96*(B3), 4435–4456. https://doi.org/10.1029/90JB02621

Kusznir, N., & Karner, G. (2007). Continental lithospheric thinning and breakup in response to upwelling divergent mantle flow: Application to the Woodlark, Newfoundland and Iberia margins. *Geological Society, London, Special Publications*, *282*(1), 389–419. https://doi.org/10.1144/SP282.16

Le Pourhiet, L., Chamot-Rooke, N., Delescluse, M., May, D. A., Watremez, L., & Pubellier, M. (2018). Continental break-up of the South China Sea stalled by far-field compression. *Nature Geoscience*, *11*(8), 605–609. https://doi.org/10.1038/s41561-018-0178-5

Little, T., Baldwin, S., Fitzgerald, P., & Monteleone, B. (2007). Continental rifting and metamorphic core complex formation ahead of the Woodlark spreading ridge, D'Entrecasteaux Islands, Papua New Guinea. *Tectonics*, *26*(1), TC1002. https://doi.org/10.1029/2005TC001911

Little, T., Hacker, B., Brownlee, S., & Seward, G. (2013). Microstructures and quartz lattice-preferred orientations in the eclogite-bearing migmatitic gneisses of the D'Entrecasteaux Islands, Papua New Guinea. *Geochemistry, Geophysics, Geosystems*, *14*(6), 2030–2062. https://doi.org/10.1002/ggge.20132

Little, T., Hacker, B., Gordon, S., Baldwin, S., Fitzgerald, P., Ellis, S., & Korchinski, M. (2011). Diapiric exhumation of Earth's youngest (UHP) eclogites in the gneiss domes of the D'Entrecasteaux Islands, Papua New Guinea. *Tectonophysics*, *510*(1–2), 39–68. https://doi.org/10.1016/j.tecto.2011.06.006

MacCready, T., Snoke, A. W., Wright, J. E., & Howard, K. A. (1997). Mid-crustal flow during Tertiary extension in the Ruby Mountains core complex, Nevada. *The Geological Society of America Bulletin*, *109*(12), 1576–1594. https://doi.org/10.1130/0016-7606(1997)109<1576:MCFDTE>2.3.CO;2

McKenzie, D. (1978). Some remarks on the development of sedimentary basins. *Earth and Planetary Science Letters*, *40*(1), 25–32. https://doi.org/10.1016/0012-821X(78)90071-7

McKenzie, D., Nimmo, F., Jackson, J. A., Gans, P., & Miller, E. (2000). Characteristics and consequences of flow in the lower crust. *Journal of Geophysical Research*, *105*(B5), 11029–11046. https://doi.org/10.1029/1999JB900446

Miller, S. R., Baldwin, S. L., & Fitzgerald, P. G. (2012). Transient fluvial incision and active surface uplift in the Woodlark Rift of eastern Papua New Guinea. *Lithosphere*, *4*(2), 131–149. https://doi.org/10.1130/L135.1

Mondy, L. S., Rey, P. F., Duclaux, G., & Moresi, L. (2018). The role of asthenospheric flow during rift propagation and breakup. *Geology*, *46*(2), 103–106. https://doi.org/10.1130/G39674.1

Morley, C. K., & Westaway, R. (2006). Subsidence in the super-deep Pattani and Malay basins of Southeast Asia: A coupled model incorporating lower-crustal flow in response to post-rift sediment loading. *Basin Research*, *18*(1), 51–84. https://doi.org/10.1111/j.1365-2117.2006.00285.x

Panien, M., Schreurs, G., & Pfiffner, A. (2006). Mechanical behaviour of granular materials used in analogue modelling: Insights from grain characterisation, ring-shear tests and analogue experiments. *Journal of Structural Geology*, *28*(9), 1710–1724. https://doi.org/10.1016/j.jsg.2006.05.004

Poppe, S., Holohan, E. P., Galland, O., Buls, N., Van Gompel, G., Keelson, B., et al. (2019). An inside perspective on magma intrusion: Quantifying 3D displacement and strain in laboratory experiments by dynamic X-ray computed tomography. *Frontiers of Earth Science*, *7*, 62. https://doi.org/10.3389/feart.2019.00062

Ramberg, H. (1981). *Gravity, deformation and the Earth's crust: In theory, experiments and geological application* (p. 452). Academic Press.

Rotevatn, A., Jackson, C. A.-L., Tvedt, A. B., Bell, R. E., & Blækkan, I. (2019). How do normal faults grow? *Journal of Structural Geology*, *125*, 174–184. https://doi.org/10.1016/j.jsg.2018.08.005

Santimano, T., Rosenau, M., & Oncken, O. (2015). Intrinsic versus extrinsic variability of analogue sand-box experiments – Insights from statistical analysis of repeated accretionary sand wedge experiments. *Journal of Structural Geology*, *75*, 80–100. https://doi.org/10.1016/j.jsg.2015.03.008

Schmid, T., Rudolf, M., Schreurs, G., Adam, J., & Rosenau, M. (2021). *3D stereo DIC data from analogue models exploring fault growth and rift propagation in rotational rift systems*. GFZ Data Services. https://doi.org/10.5880/fidgeo.2021.048

Schmid, T., Schreurs, G., Warsitzka, M., & Rosenau, M. (2020a). *Effect of sieving height on density and friction of brittle analogue material: Ring-shear test data of corundum sand used for analogue experiments in the Tectonic Modelling Lab of the University of Bern (CH)*. GFZ Data Services. https://doi.org/10.5880/fidgeo.2020.005

Schmid, T., Schreurs, G., Warsitzka, M., & Rosenau, M. (2020b). *Effect of sieving height on density and friction of brittle analogue material: Ring-shear test data of quarz sand used for analogue experiments in the Tectonic Modelling Lab of the University of Bern*. GFZ Data Services. https://doi.org/10.5880/fidgeo.2020.006

Schmid, T. C., Rudolf, M., Schreurs, G., Adam, J., & Rosenau, M. (2022). *DVC and 3D stereo DIC data from analogue models exploring interaction of viscous flow and surface deformation in rotational rift systems*. GFZ Data Services. https://doi.org/10.5880/fidgeo.2022.006

Schmid, T. C., Schreurs, G., & Adam, J. (2022). Characteristics of continental rifting in rotational systems: New findings from spatiotemporal high resolution quantified crustal scale analogue models. *Tectonophysics*, *822*, 229174. https://doi.org/10.1016/j.tecto.2021.229174

Taylor, B., Goodliffe, A. M., & Martinez, F. (1999). How continents break up: Insights from Papua New Guinea. *Journal of Geophysical Research*, *104*(B4), 7497–7512. https://doi.org/10.1029/1998JB900115

Turcotte, D. L., & Schubert, G. (1982). *Geodynamics: Applications of continuum physics to geological problems* (p. 450). John Wiley & Sons.

Van Wijk, J., & Blackman, D. (2005). Dynamics of continental rift propagation: The end-member modes. *Earth and Planetary Science Letters*, *229*(3–4), 247–258. https://doi.org/10.1016/j.epsl.2004.10.039

Wallace, L. M., Ellis, S., Little, T., Tregoning, P., Palmer, N., Rosa, R., et al. (2014). Continental breakup and UHP rock exhumation in action: GPS results from the Woodlark Rift, Papua New Guinea. *Geochemistry, Geophysics, Geosystems*, *15*(11), 4267–4290. https://doi.org/10.1002/2014GC005458

Wallace, L. M., Stevens, C., Silver, E., McCaffrey, R., Loratung, W., Hasiata, S., et al. (2004). GPS and seismological constraints on active tectonics and arc-continent collision in Papua New Guinea: Implications for mechanics of microplate rotations in a plate boundary zone. *Journal of Geophysical Research*, *109*(B5), B05404. https://doi.org/10.1029/2003JB002481

Wernicke, B. (1985). Uniform-sense normal simple shear of the continental lithosphere. *Canadian Journal of Earth Sciences*, *22*(1), 108–125. https://doi.org/10.1139/e85-009

Westaway, R. (1994). Re-evaluation of extension across the Pearl River Mouth Basin, South China Sea: Implications for continental lithosphere deformation mechanisms. *Journal of Structural Geology*, *16*(6), 823–838. https://doi.org/10.1016/0191-8141(94)90148-1

Westaway, R. (2005). Active low-angle normal faulting in the Woodlark extensional province, Papua New Guinea: A physical model. *Tectonics*, *24*(6), TC6003. https://doi.org/10.1029/2004TC001744

Zuber, M., Parmentier, E., & Fletcher, R. (1986). Extension of continental lithosphere: A model for two scales of Basin and Range deformation. *Journal of Geophysical Research*, *91*(B5), 4826–4838. https://doi.org/10.1029/JB091iB05p04826

Zwaan, F., & Schreurs, G. (2020). Rift segment interaction in orthogonal and rotational extension experiments: Implications for the large-scale development of rift systems. *Journal of Structural Geology*, *140*, 104119. https://doi.org/10.1016/j.jsg.2020.104119

Zwaan, F., Schreurs, G., & Adam, J. (2018). Effects of sedimentation on rift segment evolution and rift interaction in orthogonal and oblique extensional settings: Insights from analogue models analysed with 4D X-ray computed tomography and digital volume correlation techniques. *Global and Planetary Change*, *171*, 110–133. https://doi.org/10.1016/j.gloplacha.2017.11.002

Zwaan, F., Schreurs, G., & Buiter, S. J. H. (2019). A systematic comparison of experimental set-ups for modelling extensional tectonics. *Solid Earth*, *10*(4), 1063–1097. https://doi.org/10.5194/se-10-1063-2019

Zwaan, F., Schreurs, G., Ritter, M., Santimano, T., & Rosenau, M. (2018). *Rheology of PDMS-corundum sand mixtures from the Tectonic Modelling Lab of the University of Bern (CH)*. GFZ Data Services. https://doi.org/10.5880/fidgeo.2018.023

Zwaan, F., Schreurs, G., & Rosenau, M. (2020). Rift propagation in rotational versus orthogonal extension: Insights from 4D analogue models. *Journal of Structural Geology*, *135*, 103946. https://doi.org/10.1016/j.jsg.2019.103946